Modeling Inner Boundary Values at 18 Solar Radii During Solar Quiet time for Global Three-dimensional Time-Dependent Magnetohydrodynamic Numerical Simulation

Chin-Chun Wu[1], Kan Liou[2], Brian E. Wood[1], Simon Plunkett[3], Dennis Socker[1], Y.M. Wang[1], S. T. Wu[4], Murray Dryer[5], and Christopher Kung[6]

[1] Naval Research Laboratory, Washington, DC 20375, USA
[2] Applied Physics Laboratory, Johns Hopkins University, Laurel, Maryland, USA
[3] NASA, Washington D.C, USA
[4] CSPAR, University of Alabama, Huntsville, Alabama, USA (Deceased)
[5] Emeritus, NOAA, Boulder, Colorado, USA
[6] Engility Corporation, HPCMP PETTT, NRL, Code 5590, 4555 Overlook Ave, SW, Washington, DC 20375, USA

09-Jan-2020

***Key Words: Global 3D MHD simulation, Space Weather Prediction, Interplanetary Shock, CME, Geomagnetic Storm**

Abstract

We develop an empirical model of the solar wind parameters at the inner boundary (18 solar radii, R_s) of the heliosphere that can be used in our global, three-dimensional (3D) magnetohydrodynamic (MHD) model (G3DMHD) or other equivalent ones. The model takes solar magnetic field maps at 2.5 R_s, which is based on the Potential Field Source Surface, PFSS model and interpolates the solar wind plasma and field out to 18 R_s using the algorithm of Wang and Sheeley [1990]. A formula ($V_{18Rs} = V_1 + V_2 f_s^{\alpha}$) is used to calculate the solar wind speed at 18 R_s, where V_1 is in a range of 150-350 km/s, V_2 is in the range of 250-500 km/s, and "f_s" is the magnetic flux expansion factor derived from the Wang and Sheeley (WS) algorithm at 2.5 R_s. To estimate the solar wind density and temperature at 18 R_s, we assume an incompressible solar wind and a constant total pressure. The three free parameters are obtained by adjusting simulation results to match in-situ observations (*Wind*) for more than 54 combinations of V_1, V_2 and α during a quiet solar wind interval, *i.e.*, the Carrington Rotation (CR) 2082. We found that V_{BF} = (200±50) + (400±100) $f_s^{-0.4}$ km/s is a good formula for the quiet solar wind period. The formula was also good to use for the other quiet solar periods. Comparing results between WSA [Arge *et al.* 2000; 2004] and our model (WSW-3DMHD), we find the following: i) The results of using V_{BF} with the full rotation (FR) data as input to drive the 3DMHD model is better than the results of WSA using FR, or daily updated. . ii) The WSA model using the modified daily updated 4-day-advanced solar wind speed predictions is slightly better than that for WSW-3DMHD. iii) The results of using V_{BF} as input to drive the 3DMHD model is much better than the using the WSA formula with an extra parameter for the angular width (θ_b) from the nearest coronal hole. The present study puts in doubt in the usefulness of θ_b for these purposes.

1. Introduction

Predictions of the arrival time of geoeffective solar events, such as coronal mass ejections (CMEs), at an observer's location in the heliosphere is one of the most daunting challenges of space science applications. When a CME erupts and moves into the solar wind, it is known as an interplanetary coronal mass ejection (ICME) [Dryer *et al.* 1994]. A fast-mode shock may result at the leading edge of the CME front, which may itself be geoeffective [*e.g.*, Gosling *et al.,* 1975; Sheeley *et al*., 1982]. Observations have shown that a large percentage of ICMEs classified as "magnetic clouds" (MCs), especially those with a leading shock, can lead to geomagnetic storms [*e.g*., Wu and Lepping, 2002; Huttunen *et al*. 2005; Zhang *et al*. 2007].

Knowledge about when and if any part of the shock and ICME will reach the Earth can be used as a harbinger of geomagnetic activity. Interactions of CMEs with the solar wind complicates predictions of their arrival. Because of the interaction, the propagating speed of CMEs approaches the ambient solar wind speed [Gopalswamy *et al.* 2000]. Therefore, being able to predict the solar wind speed is a prerequisite for accurately predicting the arrival time of CMEs.

First principle models that employ magnetohydrodynamic (MHD) theory have been developed for simulating the dynamics of the Sun and the heliosphere. Han *et al.* [1988] developed the first numerical time-dependent, three-dimensional (3-D), MHD simulation model. The model is able to simulate interplanetary (IP) shock evolution from 18 solar radii (R_s) or 0.1 AU, to the Earth [*e.g.,* Han *et al.* 1988; Detman *et al.* 1991; Dryer *et al.* 1997; Wu and Dryer, 1997; Wu *et al.* 1996; 2005]. We will refer this model as Han's code hereafter. Han's code has also been used previously to study (i) the interplanetary magnetic field (IMF) draping around plasmoids in the solar wind [Detman *et al.,* 1991]; (ii) IMF changes at 1 AU as a consequence of an interaction with a heliospheric current/plasma sheet (HCS/HPS) [Wu *et al.* 1996; Wu and Dryer, 1997]; and (iii) the shock arrival time at the Earth [Wu *et al.* 2005]. Several early examples include evolution of a shock driven by a CME that occurred on 14 April 1994, and its propagation to the Earth and at ~4 AU [Dryer *et al.* 1997]. Pressure pulses have also been utilized at lower boundaries to mimic solar events to study the evolution of solar transient disturbances (*e.g.*, shocks, plasma clouds, and magnetic flux ropes) by other groups [*e.g.*, Odstrcil and Pizzo, 1999a,b; Groth *et al.* 2000; Hayashi *et al.* 2011; Manchester *et al.* 2004; Vandas *et al.* 2002; Luguz *et al.* 2011; Shen *et al.* 2011].

Potential Field Source-Surface (PFSS) models are often used to derive ambient solar wind parameters at the inner boundary of heliospheric MHD models [*e.g.* Usmanov 1993; Manchester *et al.* 2004; Odstrcil *et al.* 2005; Detman *et al.* 2006; Luguz *et al.* 2011; Shen *et al.* 2011; Wu *et al.* 2007a,b]. With PFSS providing the inner boundary conditions, Han's code and the Hakamada, Akasofu and Fry (HAF) code [Fry *et al.* 2001] were merged as a hybrid model (HAF+3DMHD) to simulate realistic solar wind structures from 2.5 R_s to the Earth environment and beyond [Liou *et al.* 2014; Wood *et al.* 2011, 2012; Wu *et al.* 2007a,b, 2011, 2012, 2016a,b]. The combined HAF+3DMHD model is capable of simulating extremely fast CME events, such as the CME that erupted on 23 July 2012 with a shock speed (V_S) faster than 3000 km/s [Liou *et al.,* 2014]. It is also capable of modeling the evolution and interaction of multiple CMEs [*e.g.*, Wu *et al.* 2012; Wu *et al.* 2016b; S.T.Wu *et al.* 2014].

Using 22 years of flux-tube expansion factor measurements (f_s, derived near the Sun), Wang and Sheeley [1990] constructed an empirical model for estimating the daily characteristic solar wind speed at the Earth (WS model) based on f_s. These linkage of the two quantities is affected by the time required for the radially propagating solar wind (assumed to be flowing at constant velocity) to traverse from Sun to Earth.

The velocity profile produced by the WS velocity scheme is discretized rather than continuous. Therefore, the WS velocity relationship is not ideal as input for the global MHD simulation. Arge and Pizzo [2000] (AP) made a number of modifications to the basic technique of the WS model. The AP v-f_s relationship is a continuous empirical function that related magnetic expansion factor to solar wind velocity at the source surface. The AP v-f_s relationship used daily updated synoptic maps instead of full-rotation maps. Both WS and AP v-f_s relationship use solar wind speed at the first Lagrangian (L1) to trace back to the solar source surface. The solar wind speed is highly non-uniform near the Sun.

The ambient (pre-existing background) solar wind speed is known to affect the acceleration and deceleration of CMEs [*e.g.*, Gopalswamy *et al*. 2009; Wu, Lepping, and Gopalswamy, 2006]. Time-dependent, 3D MHD simulations also show that the background solar wind can affect the arrival time of shock events with slow propagation speed (V_{Shock} < 100 km/s) but not shock events with fast propagation speed [*e.g.,* Wu *et al.* 2005].

Current 3D global MHD models often overestimate the background solar wind speed at the inner boundaries, *e.g*., works performed by Wu *et al.* [2016a,b] with the HAF+3DMHD model and by Yu *et al*. [2015] with the ENLIL model using solar wind solar wind velocities derived from interplanetary scintillation (IPS) measurements. In their simulation using the ENLIL model, Yu *et al.* had to reduce the solar wind speed input at 0.1 AU by ~20% to get the right IP shock arrival time at the Earth. For space weather forecasting purposes, it is important to be able to obtain the correct initial solar wind speed as a simulation input. Therefore, we are motivated to develop a scheme for providing solar wind velocities at the inner boundary (18 R_s) for three-dimensional, time-dependent MHD simulation models, which can then predict realistic background solar wind conditions at Earth.

The remaining sections of the paper are organized as follows. We will describe the numerical simulation in Section 2. In Section 3, we demonstrate the methodology. Tuning the model, including validation of simulation results (*i.e.*, parameter tuning for 1 AU solar wind speed), is described in Section 3. Discussion, Conclusions and Remarks are given in Section 4.

2. Global Three-Dimensional MHD Simulation Model (G3DMHD)

2.1 3-D MHD simulation model

The fully 3-D, time-dependent MHD simulation code [Han, 1977; Han *et al*. 1988] was used to propagate solar wind parameters at the inner boundary to 1 AU to compare with *in situ* measurements. The MHD model solves a set of ideal-MHD equations using an extension scheme of the two-step Lax-Wendroff finite difference methods [Lax and Wendroff, 1960]. An ideal MHD fluid is assumed in the Han model, which solves the basic conservation laws (mass, momentum, and energy) as shown in Equations (1) - (3) with the induction equation (Equation 4) to take into account the nonlinear interaction between plasma flow and magnetic field.

$$\frac{D\rho}{Dt} + \rho\nabla \bullet \mathbf{V} = 0 \tag{1}$$

$$\rho\frac{D\mathbf{V}}{Dt} = -\nabla p + \frac{1}{\mu_o}(\nabla\times\mathbf{B})\times\mathbf{B} - \rho\frac{GM(r)}{r^2}\hat{\mathbf{r}} \tag{2}$$

$$\frac{\partial}{\partial t}[\rho e + \frac{1}{2}\rho|\mathbf{V}|^2 + \frac{|\mathbf{B}|^2}{2\mu_o}] + \nabla\bullet[\mathbf{V}\{\rho e + \frac{1}{2}\rho|\mathbf{V}|^2 + p\} + \frac{\mathbf{B}\times(\mathbf{V}\times\mathbf{B})}{\mu_o}] = -\mathbf{v}\bullet\rho\frac{GM(r)}{r^2}\hat{\mathbf{r}} \tag{3}$$

$$\frac{\partial\mathbf{B}}{\partial t} = \nabla\times(\mathbf{V}\times\mathbf{B}) \tag{4}$$

where t, r, ρ, V, B, p, e are time, radius, density, velocity, magnetic field, thermal pressure, and internal energy. The internal energy is $e \equiv p/[(\gamma-1)\rho]$. The additional symbols γ, M_s, G are the polytropic index, the solar mass, and the gravitational constant. A value of $\gamma = 5/3$ is used for this study since it has been shown to be a good value to use for in-situ solar wind data at 1 AU [*e.g.* Wu *et al.,* 2011; Liou *et al.,* 2014]. The MHD governing equations are cast in uniform, spherical grids. The computational domain for the 3-D MHD simulation is a sun-centered spherical coordinate system (r, θ, ϕ) oriented on the ecliptic plane. Earth is located at $r = 215\ R_s$, $\theta = 0^o$, and $\phi = 180^o$. The domain covers $-87.5^o \le \theta \le 87.5^o$; $0^o \le \phi \le 360^o$; $18\ R_s \le r \le 345\ R_s$. An open boundary condition at both $\theta = 87.5^o$ and $\theta = -87.5^o$ is used so there are no reflective disturbances. A constant grid size of $\Delta r = 3\ R_s$, $\Delta\theta = 5^o$, and $\Delta\phi = 5^o$ is used, which results in 110×36×72 grid sets.

2.2 Inner Boundary Data Set Up

The system is driven by a time series of photospheric magnetic maps composed from daily solar photospheric magnetograms (http://wso.stanford.edu). The WS model uses the observed line-of-sight magnetic field at the photosphere extrapolated to 2.5 R_s using the PFSS model [*e.g.*, Wang and Sheeley, 1992]. The inner boundary of the 3-D MHD model is at an adjustable location, typically beyond the critical points at 18 solar radii (R_s). The conservation of magnetic flux ($r\ B_r^2$ = constant) is used to derive magnetic field at 18 R_s. Conservation of the flux tube $r\ B_r^2$ = constant is assumed to set up spacing variation (*i.e.* grid size) in both θ- and ϕ-direction. A formula $V_r = V_1 + V_2 f_s^{\alpha}$ (units in km/s) is used to compute Vr at 18 R_s, where V_1 is a constant ranging from 150 to 350, V_2 is also a constant ranging from 250 to 500, f_s is the expansion factor [Wang and Sheeley, 1990; Wang *et al.* 1990, 1992], and α is the exponent of the expansion factor. This is similar to the work done by Arge *et al.* [2004]. Conservation of mass, $\rho V = \rho_o V_o$ = constant, is used to compute the solar wind density at 18 R_s, where ρ_o is 2.35x10^{-9} kg/km^3 and V_o is the average of V_r at 18 R_s. We further assume that the total pressure is constant along the stream line (Bernoulli's principle). The equation $\rho\ (RT + v^2/2) = \rho_o\ (RT_o + v_o^2/2)$ = constant is used to compute the temperature at 18 R_s, where $T_o = 1.5 \times 10^6$ °K is used at 18 R_s.

2.3 Selection of Study period

The occurrence frequency of CMEs ranges from ~0.6/day to ~4/day [*e.g.,* Wu, Lepping, and Gopalswamy, 2006] or to ~6/day [Wang and Colaninno, 2014; Hess and Colaninno, 2017; Vourlidas *et al.* 2017], depending on the phase of the solar cycle. When a CME/ICME/Shock propagates from the Sun to the Earth, the ambient solar wind can vary a lot, depending on the size/speed of the CME. For constructing a global MHD simulation model, a quiet solar wind period is a better choice to test the model. Therefore, we picked a quiet period (*i.e.* sunspot number, SSN is small) during which the occurrence frequency of CMEs is also low. The value of the 13-month smoothed monthly total SSN is 3.4 in April-May 2009 (http://www.sidc.be/silso/datafiles). No MCs were observed during April - May 2009 [Lepping *et al.* 2015]. In addition, no magnetic cloud like structure was found in 2009 [Wu and Lepping, 2015]. Therefore, Carrington Rotation (CR) 2082 (April 5 to May 3, 2009) was chosen to test our new solar wind speed scheme under quiet conditions.

Figure 1 shows the background (co-rotating "steady state") solar wind radial speed (V_r) on the surface plane at 18 and 216 R_s at 02:00UT on 3 April 2009. These values are calculated using $Vr = 150 + 250 f_s^{-0.4}$ (Fig. 1a-b) and $Vr = 150 + 500 f_s^{-0.4}$ (Fig. 1c-d). The solar wind speed is faster at 216 R_s (see Fig. 1b and 1d) than that at 18 R_s (see Fig. 1a and 1c). Overall, Figure 1 clearly shows that solar wind speed using the formula $Vr = 150 + 500f_s^{-0.4}$ is faster than that obtained by using the formula $Vr = 150 + 250f_s^{-0.4}$.

2.4 **Setting up co-rotating steady state solar wind.**

The governing MHD equations are described in the inertial frame. Thus, the solar sidereal rotation vector, Ω, does not appear in the governing equations. Instead of using the rotating frame as the reference coordinate system, we assume that the distribution map of the inner boundary values at 18 R_s moves longitudinally at the solar sidereal rotation rate in the inertial system. We set the solar rotation rate |Ω| to be 360 degrees per 27.27 days. On 2 April 2009, the Earth was located at a latitude of south 6.6° (S6.6°) with respect to the solar equator. Figure 2 shows the velocity profile at 2.5° south (S2.5°) of the solar-equatorial plane using the formula, $Vr = 150 + 300f_s^{-0.4}$ for the velocity map at 18 R_s. Initially, there is no spiral structure in the solar wind (Figure 2a); so everything goes out radially. When the solar rotation is applied to the simulation domain, the spiral structure appears (Figures 2b-f). It takes ~4 days for the spiral configuration to reach 1 AU (Figure 2d) and ~6 days for the spiral configuration to reach the outer boundary of the simulation domain (Figure 2e).

Figure 1 clearly shows a non-uniform 2-D velocity profile at 18 R_s in both θ-, and ϕ-directions. The flow speed is larger in the high-latitude than in the low-latitude regions, as is expected from the expansion factor, which is smaller in the high-latitude corona hole regions and larger in the low-latitude closed field regions. Figures 3a-3d and 3e-3h show the simulated solar wind speed and density on surfaces of different angular cones centered at the Sun. These conical angles are at 22.5ºN (north, representative of a response in the northern heliosphere), 7.5ºN, 7.5ºS (close to Earth's latitude in the solar equatorial coordinate system), and 22.5ºS (south, representative of a response in the southern heliosphere). Figures 3i-3m show the solar wind speed at different longitudinal meridian planes: 90ºE (East, Fig.3i), 45ºE (Fig.3j), 0ºW (west, Fig.3k, Sun-Earth-line direction), 45ºW (Fig.3l), and 90ºW (Fig.3m).

The solar wind speed profiles are highly non-uniform. For example, i) The solar wind is slower at the inner boundary (*i.e.* 18 R_s) and is faster at 1 AU (*i.e.* 215 R_s), meaning that the solar wind must have experienced acceleration beyond 18 R_s; ii) the solar wind iss faster in the Southern Hemisphere and slower in the Northern Hemisphere; iii) The highest speed stream was located near 180ºW in the Southern Hemisphere but near the 5ºW in the Northern Hemisphere; iv) The solar wind is slower near the equator than in the high-latitude regions (See Fig. 3a-3d, and 3i-3m).

3. Validation of Simulation Results

3.1 Effect of V_1 and V_2 on the solar wind profile

The solar wind condition at 18 R_s is set up with the WS formula: $V_1 + V_2 f_s^{-0.4}$ km/s. In general, V_1 is the baseline solar wind speed and V_2 is the amplitude of the solar wind speed above the baseline. While other empirical formulas have been proposed, such as the WSA model (2000), in this study, we mainly concentrate on testing the WS formula. The expansion factor (f_s) is calculated based on the solar magnetogram measurements from the Wilcox Solar Observatory (WSO), in conjunction with the PFSS model (Wang and Sheeley, 1990). We perform simulations with fifty-four different cases (combinations of V_1 and V_2) to determine the optimal values for V_1 and V_2. The value of V_1 ranges between 150 and 350 km s^{-1} in increments of 25 km s^{-1} (*top to bottom,* panels, **1 – 9**) and the value of V_2 ranges from 250 to 500 km s^{-1} in increments of 50 km s^{-1} (*left to right,* panels **A – F**). Simulation results at 1 AU are compared with in situ observations by *Wind*. A number of metrics are considered to determine the strength of the predictions: the Pearson correlation coefficient [cc], the difference between $<V>_{\mathrm{OMNI}}$ and $<V>_{\mathrm{3DMHD}}$ (Diff ≡ ($<V>_{OMNI}$ - $<V>_{\mathrm{3DMHD}}$) / $<V>_{\mathrm{OMNI}}$), the average simulated solar wind speeds ($<V>_{\mathrm{3DMHD}}$), the mean absolute percentage error [MAPE ≡ $100/N \times \sum |(\mathrm{V}_{Wind} - \mathrm{V}_{\mathrm{G3DMHD}})/\mathrm{V}_{wind}|$], and the ratio of the correlation coefficient to MAPE (cc/MAPE). These metrics are marked on the top of each panel (see Figure 4 caption for details). For example, for the case A1 (the top-left corner), $V_{18R_s} = 150 + 250 f_s^{-0.4}$, the values of cc, Diff, $<V>_{\mathrm{3DMHD}}$, cc/MAPE, and MAPE are 0.72, -7 %, 362, 7.5, and 9%, respectively. Time profiles of solar wind speed at the Earth for the period between March 30 and April 27, 2009 for 27 out of 54 cases are presented in Figure 4. From top to bottom (Panels 1 to 9): V_1 was 150, 175, 200, 225, 250, 275, 300, 325, and 500 km/s, respectively. From left to right: V_2 was 250, 300, 350, 400, 450, and 500, respectively.

Overall, during March 20-April 27, 2009, Case F1 ($Vr = 150 + 500 f_s^{-0.4}$) has the best correlation coefficient (=0.80) and also has a very low difference (= 1%). Case F2 ($Vr = 175 + 500 f_s^{-0.4}$) also has a good fit, except the difference is 5% higher than that for Case F1. Other cases also have a high correlation coefficient and a low difference, but the trend is not as good as Case F1, *i.e.* matched velocity profile for both velocity in the minimum ($V_{\min}$, minimum velocity) and maximum ($V_{\max}$, maximum velocity). For example, $V_{\max}$ is far off the observation in either Case A3 ($Vr = 250 + 250 f_s^{-0.4}$, cc =0.78, Diff =1%), or Case C2 ($Vr = 250 + 350 f_s^{-0.4}$, cc =0.78, Diff =0%). Figure 5 shows the contours of correlation coefficients for the 54 cases. The values of the correlation coefficients were in a range of 0.56-0.79; and the differences were in a range of -7% to 56%, respectively. Colors and red contours represent cc x 100 (units in %). Light-blue-dashed contours represent differences between $<V_{\mathrm{obs.}}>$ and $<V_{\mathrm{G3DMHD}}>$, which equals to ($<V_{\mathrm{G3DMHD}}>$ - $<V_{\mathrm{obs}}>$)/$<V_{\mathrm{obs.}}>$ x 100.

Using the velocity formula $V_{18R_s} = V_1 + V_2 f_s^{-0.4}$ to construct solar wind speed (see Figures 4-5) at the inner boundary, two major trends of solar wind speed near the Earth are identified: (i) the baseline solar wind speed was low if a low value of V_1 is used. (ii) The peak solar wind speed (V_{peak}) is high if a large value of V_2 is used. The trend of the speed variation is similar between the observations and the simulations for cases with V_1 less than 225 km/s (Panels 5-9). For cases with a high value of V_1 (*i.e.,* $V_1 > 250$ km/s), the simulated speed baselines were much higher than observed (see panels 6-9 of Figure 4). Overall the equation $V_{18R_s} = (200\pm50) + (400\pm100)\, f_s^{-0.4}$ is a good fit to background solar wind at 1 AU.

We first draw attention to the comparison of the simulation results with the *in-situ* observations at Earth in Figure 6. The equations $Vr=150+250f_s^{-0.4}$ and $Vr=150+500f_s^{-0.4}$ were used to produce the background solar wind in Figures 6a and 6b, respectively. The time resolution of the observations is ≈1.5 minutes. The time resolution of the simulated solar wind is in a range of 1-15 minutes, which depends on the simulated solar wind condition. Both data sets were interpolated into hourly resolution. Validation of our simulation results was done by comparing solar wind plasma and field parameters with *in situ* measurements at 1 AU (*e.g,* made by *Wind* or *ACE* spacecraft, or *OMNI* data set).

Figure 6 shows a comparison of the solar wind parameters from G3DMHD simulations (black-solid-lines) and *in situ* observations (*OMNI*, red-dotted-lines) during March 30 - April 27, 2009 for Cases 1a ($Vr=150+250f_s^{-0.4}$, Fig.6a) and 1c ($Vr=150+500f_s^{-0.4}$, Fig.6b). Panels from top to bottom show the time profile of solar wind temperature (*Tp*, units in °K), velocity in r-direction (*Vr*, units in km/s), density (*Np*, units in cm^{-3}), and magnitude of interplanetary magnetic field (*B*, units in nT). Earth was orbiting between 6.7° and 5.0° below the solar equatorial plane (or S6.7° and S5.0°).

For the case of Vr = 150+250$f_s^{-0.4}$ (Case 1a), the averages of ambient solar wind parameters <*Tp*>, <*Vr*>, and <*Np*> were under-estimated by ~28%, 7%, and 28%, respectively (see Fig.6a); but the average of total magnetic field, <*B*> was over-estimated by 15%. The cc's for simulation vs. observation were 0.71, 0.72, 0.56, 0.02 for *Tp*, *Vr*, *Np*, and *B*, respectively.

For the case of Vr = 150+500$f_s^{-0.4}$ (Case 1c), ambient solar wind <*Tp*> and <*Np*> were under-estimated by 22% (-22%) and 12% (-12%), respectively (See Fig. 6b); but <*Vr*> and <*B*> were over-estimated by 1% and 37%. The cc's for simulation *vs.* observation are 0.63, 0.79, 0.73, and 0.28 for *Tp*, *Vr*, *Np*, and *B*, respectively. Overall, the results for Case 1c are better than that for Case 1a.

3.2 Effect of expansion factor on the profile of solar wind speed

The velocity formula $Vr = V_1+V_2 f_s^{\alpha}$ has three free variables, V_1, V_2, and α. The V_1 and V_2 parameters were tested in the above section. Here, the effects of α will be determined. Figure 7 shows solar wind variations with different values of α: -0.1 (Fig.7a), -0.2 (Fig.7b), -0.4 (Fig.7c), and -0.6 (Fig.7d) for the period of CR2082 by using different velocity formulae with different values of α:(a) $Vr = 150 + 500f_s^{-0.1}$, (b) $Vr = 150 + 500f_s^{-0.2}$, (c) $Vr = 150 + 500f_s^{-0.4}$, and (d) $Vr = 150 + 500f_s^{-0.6}$. The cc's for these four cases are 0.55, 0.67, 0.79, and 0.78. On average, the solar wind speed was 8% under-estimated by using formula (d), but were 48%, 25%, 1% over-estimated by using formula (a), (b), and (c), respectively. Figure 7 shows clearly that α affects the baseline speed of the solar wind. In other words, a low value of α results in a slow background solar wind. Formula (d) is a good fit to the data except for the peak speed, which is under-estimated by ~100 km/s. The velocity profile derived from formula (c), $Vr = 150 + 500f_s^{-0.4}$, is one of the best choices for this period. The best-fit α parameter is obtained by fixing the V_1

and V_2 values. Although a more general approach is to consider all three free parameters together in the fit, this would require considerable computing resources. This will be a future study topic.

3.3 Validation of the best fit formula, V = 150 + 500 $f_s^{-0.4}$

Figure 4 shows the best fit formula ($V_{BF} = 150 + 500\ f_s^{-0.4}$) for CR2082. The V_{BF} empirical formula used in the study is similar to those used in the study of Arge and Pizzo [2000]. The main result of the present study (a formula with best-fit parameters) is nearly identical to the Equation (4) in the paper of Arge and Pizzo [2000], except with a lower value of V_1, and a higher value of V_2 [Arge and Pizzo, 2000] (refer to AP hereafter). They used three different source surface maps: (i) the full rotation (FR), (ii) daily updated (DU), and (iii) modified daily updated (MDU) 4-day-advanced solar wind speed predictions with 9-hour-averaged WIND satellite velocity observation for CR1899. The correlation coefficients for Wind in-situ solar wind speed data vs. AP's predicted solar wind speed are 0.678, 0.793, and 0.813 for using FR, DU, and MDU data sets, respectively (see Figure 4 in AP).

In order to evaluate our formula (**V = 150 + 500** $\boldsymbol{f_s^{-0.4}}$), it is used to simulate the solar wind

condition for CR1899 during 6 August – 3 September, 1995. A comparison of the full rotation G3DMHD/simulated solar wind V (top panel), Np (second panel from top), Tp (third panel from top), and B (bottom panel) with 9-hour-averaged *WIND* spacecraft solar wind observations (red dotted lines) are showed in Figure 7. The correlation coefficient (CC) is 0.803 for simulated velocity vs. *Wind in-situ* observation. The mean absolute percentage error (MAPE) [≡ $(100/N\sum |V_{WIND} - V_{G3DMHD})/V_{WIND}|$] is 12.4%, and the average deviation is ~49.4 km/s. Our result is better than AP's results using the full rotation (FR) data or the daily updated (DU) data.

However, the cc is slightly less than AP's results of using modified daily updated (MDU) 4-day-advanced solar wind speed. Values of cc for simulation vs. observation are 0.48, 0.63, and -0.04 for Np, Tp, and B, respectively. Values of the MAPE are 0.01, 0.336, and 0.439 for Np, Tp, and B, respectively. We have to stress that a better linear correlation is not necessarily a better fit. This is the reason that we use MAPE to evaluate the fit.

In this study we have carefully selected a period without any solar disturbance, and used about 54 different combinations of simple velocity empirical formula to find a best fit formula in a solar quiet time. In the above paragraph, we demonstrated that the simple formula, V_{BF}, is also valid in 1995, which is at the end of solar cycle 22. Riley *et al.* [2001] used a θ_b parameter, in addition to f_s, to empirically specify solar wind speed near the Sun for a number of years, where θ_b is the minimum angular separation (at the photosphere) between an open field foot point and its nearest coronal hole boundary, as introduced by Arge *et al.* [2003]. Their predicted velocity for CR 1921-1923 was shown in Fig. 3 of Arge *et al.* [2004]. It is clearly shown that their prediction for CR1922 during the three-day period (May 8-11, 1997) was not correct. The WSA model predicted a fast stream during these three days. They claimed that using higher resolution maps may help to reduce some of these problems. In addition, WSA also made a false prediction of two high-speed streams during April 25-30, 1997. A high-speed stream observed by WIND during April 10-15 (in CR1921) was also missing from the WSA prediction. The stream during April 10-15 was caused by the crossing of an ICME, presumably associated with a CME that occurred on April 7 (Webb *et al.* 2000; Arge *et al.* 2004).

In order to further explore the capability of the V_{BF} formula for predicting the background solar wind, we consider the following three periods of solar rotation: CR1921, CR1922, and CR1923. The comparison of the WSW-3DMHD simulated solar wind speed (black solid lines) with the *Wind* in-situ solar wind speed (red-dotted lines) is shown in Figure 8. The relationship between the observation and simulation is reasonably acceptable for the periods of CR1921 and CR1923, with MAPE value of 14.9% and 17.1%, respectively. The performance is clearly much better for CR1922 (cc=0.80, MAPE = 11.6%). WSW-3DMHD correctly predicted the two fast streams during April 30 – May 03, and May 15-18 (see middle panel of Figure 9). Furthermore, WSW-3DMHD did not make the false prediction for the period of May 8-11, 1997 as did Arge *et al.* [2004].

For CR1921, WSW-3DMHD did not predict the fast solar wind profile during April 10-17, which was caused by a MC crossing starting on April 11; neither did Arge *et al.* [2004]. The V_{BF} formula is modeled with quiet solar wind parameters and therefore it fails to predict solar wind disturbances caused by the crossing of the coronal mass ejection and its driven shock. To predict such a solar wind disturbance, a proper solar disturbance is required to add into the inner boundary of the simulation. In the following section, we will demonstrate the input requirement of solar disturbance for the solar wind condition.

3.4 Validation of the best fit formula during non-quiet solar period

In this Section, we test the capability of the V_{BF} formula in solar active periods and the effect of solar disturbance (e.g., CME and its driven shock) on the solar wind profile. Two CMEs that occurred in September 2017 are simulated. Many CMEs were observed in early September 2017. STEREO-A recorded two Sun-Earth directed CMEs, which occurred on 2017-09-04 (referred as CME04) and 2017-09-06 (referred as CME06). The average CME propagating speed in the field of view (FOV) of STEREO-A for the CMEs on the 4th and 6th were 866 km/s and 1308 km/s, respectively. A pressure pulse is inserted into the lower boundary of the simulation domain to simulate the CMEs.

A comparison of the observed solar wind (speed, density, temperature, and magnetic field) with the simulation without and with a CME perturbation input is shown in Figure 10A (left panel) and 10B (right panel) between 05-09-2017 and 03-10-2017, respectively. For the case without a CME perturbation, the correlation coefficient is 0.646, 0.53, 0.38, and 0.28 for N, Np, Tp, and B, respectively. The value of MAPE is 20.7%, 0.5%, 32.5%, and 39.3% for V, Np, Tp, and B, respectively. The simulated Np, Tp, and B match well with the basic trends of observation (see 2^{nd}, 3^{rd}, and 4^{th} panels of Fig. 10A). However, the simulated velocity is far off of the observation (see top panel of Fig. 10A). Therefore, we conclude that WSW-3DMHD is not able to predict the fast streams in September 2017. Figure 10A shows that the simulated undisturbed solar wind speed was slower than the observed 500 km/s between 05-09-2017 and 03-10-2017. All the high-speed solar wind streams are not predicted by the WSW-3DMHD. One might question the prediction capability of WSW-3DMHD during the non-quiet solar period. Note that the V_{BF} was introduced to re-produce background solar wind condition in a quiet period. STEREO-A had recorded two Sun-Earth-directed CMEs on 04-09-2017 and 06-09-2017. Perturbations of these two CMEs were inserted into the lower boundary of the WSW-3DMHD.

Figure 10B shows a similar comparison as Figure 10A but with pressure pulse perturbations in the simulation. The correlation coefficient is 0.705, 0.65, 0.75, and 0.14 for V, Np, Tp, and B, respectively. The value of MAPE is 16.6%, 0.4%, 112.7%, and 66.3% for V, Np, Tp, and B, respectively. The two vertical blue dotted lines in Figure 10B indicate the arrival time of interplanetary shocks at the *WIND* spacecraft on 06-09-2017 (referred to Shock06) and 07-09-2017 (referred to Shock07). The simulated solar wind speed at both upstream and downstream of

Shock06 matches very well with the observation (see top panel of Fig. 10B). The simulated upstream speed of Shock07 is slightly higher than the observation, but the simulated downstream speed of Shock07 matches very well with the observation for about two days. The value of B downstream of Shock06 matches very well with the observation, but is poor for Shock07. A poor simulation result of B both upstream and downstream of Shock07 may be due to the fact that our simulation does not have a flux-rope structure, a very common problem in most data-driven global MHD models. Simpler dynamic pressure pulses are often used to simulate the perturbation of CMEs instead of full flux rope structures [*e.g.,* Odstricil *et al.* 2005; Wu *et al.* 2007a,b, 2019].

The above simulation result shows clearly that V_{BF} is capable of reproducing the background solar wind in quiet solar periods. When there are CMEs, additional plasma perturbations are required at the inner boundary. Further investigation is needed to confirm the capability of the V_{BF} formula for long-term solar wind studies, and for time periods with CME events.

4. Discussion, Conclusions and Remarks

In the present study, we presented a computational scheme

for deriving the background solar wind speed, as well as other solar wind parameters, at 18 solar radii (R_s), for use in heliospheric MHD modeling. This scheme employs the conservation of mass, conservation of magnetic flux tube, and Bernoulli's principle in conjunction with the magnetic flux expansion factor derived from the Wang and Sheeley [1990] algorithm. The three free parameters (V1, V2, α) in the generic form of the WS formula :$V_{18R_s} = V_1 + V_2 f_s^{\alpha}$ are determined using MHD simulations. . We performed simulations with 54 combinations of the three parameters for CR2082 and compared simulation results with in-situ observations of the solar wind by *Wind*. It is found that the following parameter set, V_1 = 200±50, V_2 = 400±100, and a = -0.4, results in the good match between simulations and observations. Based on the results of this single Carrington rotation, the capabilities of the best fit formula ($V_{BF} = 150 + 500\, f_s^{-0.4}$) was also

validated at other times, *i.e.*, in the years of 1995, 1997, 2004, 2009, and 2017. It is found that V_{BF} is applicable to those times as well. A CME perturbation has to be added into the simulation, if transients are present in the in situ data.

In this study, we also compared our results with previous studies [Arge *et al.* 2000; 2004]. Comparisons between the two models (WSA and WSW-3DMHD) are listed as follows. a) The results that used V_{BF} as input to drive the G3DMHD model is better than the results of WSA using the full rotation (FR), or daily updated (DU) wind speeds. b) WSA using the modified daily updated (MDU) 4-day-advanced solar wind speed predictions is slightly better than that for WSW-3DMHD. c) Results of using V_{BF} as input to drive 3DMHD model is better than the WSA formula. The present study does not support the use of an extra parameter for the angular width from the nearest coronal hole.

While the present empirical formula is derived using our G3DMHD model (used briefly as mentioned earlier for WSW+3DMHD), it could be used for other similar MHD models with little to no change. This could be an interesting topic for future study. Combing the empirical formula with some conservation laws, the G3DMHD model can provide a powerful tool for space weather forecasting. In this study, several Carrington rotations were investigated and a couple of CME events were studied. A long-term study and/or a study with one or more CME events can definitely improve the validation work and will be addressed in the future.

Since the present empirical formula is derived based on a single solar rotation, it is useful to test the strength of the formula for other solar cycle periods. Here, we performed a long-term study by simulating background solar wind in the solar quiet time during 2008 (CR2066-CR2077). The same procedure described in previous section (Section 3) is adapted and the result is shown in Figure A (see Appendix, Figures A1-A12). To summarize, Table 1 lists the best-fit velocity (V_{BF}) (*e.g.*, the best fit V_1 and V_2) for two different metrics: the largest value of (i) cc/MAPE (see Table 1A), and (ii) cc/NRMSD (see Table 1B). In which cc, MAPE, and NRMSD are correlation coefficient for observation versus simulation, mean absolute percentage error, and normalized root-mean-square deviation, respectively. [$MAPE = 100\%\sum_{j=1}|(Y_j-F_j)^2/Y_j|/N$, and $NRMSD = \{\sum_{j=1}|(Y_j-F_j)^2/N\}^{1/2}/<Y_j>$, where Y_j is the actual value, F_j is the forecast value, and N is the total data points.] It clearly shows that the value of V_{BF} are different for different CR periods and different metrics (*i.e.* item i in Table 1A or ii in Table 1B). It clearly shows that the value of V_{BF} are different for different CR periods and for using different metrics. Metrics i and ii are using a similar method to determine the V_{BF}. Values of V_1 and V_2 for V_{BF} for both metrics are similar except V_1 used in metric ii is slight higher than in metric i. Both parameters, cc/MAPE and cc/NRMSD are suitable to use for space weather prediction.

Table 1A. The best choice for the three parameters with the various value of V_1 and V_2 that has the largest value of cc/MAPE.

CR-MAP	2066	2067	2068	2069	2070	2071	2072	2073	2074	2075	2076	2077
cc [a]	0.87	0.60	0.73	0.61	0.57	0.39	0.72	0.76	0.61	0.46	0.28	0.53
$(cc/MAPE)_{max}$ [b]	9.02	4.75	7.11	6.91	4.49	1.95	4.44[d]	6.51	4.30	2.72	1.38	3.69
MAPE [c]	9	12	10	8	12	19	16	11	14	16	20	14
V_1 [d]	225	225	250	250	150	275	175	150	150	150	200	150
V_2 [e]	500	500	500	450	450	350	500	500	400	450	300	400

Table 1B. The best choice for the three parameters with the various value of V_1 and V_2 that has the largest value of cc/NRMSD.

CR-MAP	2066	2067	2068	2069	2070	2071	2072	2073	2074	2075	2076	2077
$(cc/NRMSD)_{max}$ [f]	7.98	3.44	5.65	5.65	3.66	1.84	3.89[d]	5.31	3.26	2.19	1.17	2.95
NRMSD [g]	11	17	12	10	15	23	19	15	19	26	28	19
V_1 [c]	250	250	275	275	175	300	200	175	175	200	250	175

V_2 [d]	500	500	450	400	500	400	500	500	400	500	300	450

[a] Correlation coefficient for the observation versus simulation
[b] The largest value of the ratio cc/MAPE × 100 [units are %] for the different cases of $V_{BF} = V_1 + V_2 f_s^{-0.4}$
[c] MAPE ≡ mean absolute percentage error
[d] V_1 for the V_{BF}
[e] V_2 for the V_{BF}
[f] The largest value of the ratio cc/NRMSD × 100 [units are %] for the different cases of $V_{BF} = V_1 + V_2 f_s^{-0.4}$
[g] NRMSD ≡ normalized root-mean-square deviation

Figure 11 shows the values of cc/MAPE corresponding to the 54 (9x6) cases for each Carrington Rotation runs with α = -0.4. A total of 648 (12×54) cases (12 Carrington Rotations, CR2066-2077) are simulated. For CR2066, the largest value of cc/MAPE (= 9.0) within the (V_1, V_2) parameter regimes is marked with an "*" (marked on the right-bottom corner) and the associated V–f_s empirical formula ($V_{BF} = 225 + 500 f_s^{-0.4}$) is provided on the left-bottom corner. From the color contour, the V_2 parameter that can result in the largest cc/MAPE value seems to be greater than 500 km/s. Overall, a higher value of V_2 and a lower value of V_1 are preferred in order for a good match between the simulation results and the observations. In the future, we plan to perform a longer-term (*e.g.* one solar cycle or one complete magnetic solar cycle) study for this kind of research to improve the space weather prediction. In the present study, the α value is fixed to 0.4. It is expected that a different α value will result in a different optimal set of (V_1, V_2). Future work is planned in which we will consider all three free parameters (V_1, V_2, α) and the entire solar cycle, but this is outside the scope of the present study.

6. Acknowledgment

All data used in this study are obtained from the public domain. We thank the OMNI PI teams and the National Space Science Data Center at Goddard Space Flight Center, National Aeronautics and Space Administration for management and providing solar wind plasma and magnetic field data. This work was supported partially by the Chief of Naval Research (CCW, YMW, BW) and the NASA 80HQTR18T0023 (CCW), HSWO2R17-0005, and 80HRTR19T0062 (CCW, KL) grants. The work of KL was supported by the NSF grant 1743118 and NASA grant NNX14A83G to the Johns Hopkins University Applied Physics Laboratory. The authors thank Dr. Christopher Kung from Engility/DoD High Performance Computing Modernization Office PETTT program for his technical assistance in parallelizing the G3DMHD code.

References

Arge, C.N., Pizzo, V.J.: 2000, Improvement in the Prediction of Solar Wind Conditions Using Near-Real Time Solar Magnetic Field Updates, *J. Geophys. Res.* **105**, 10465, DOI: 10.1029/1999JA000262.

Arge, C.N., Odstrcil, D., Pizzo, V.J., Mayer, L.R.: 2003, Improved Method for Specifying Solar Wind Speed Near the Sun, *Proc. of the Tenth Internat. Solar Wind Confer*. **679**, 190-193, doi: 10.1063/1.1618574.

Arge, C.N., Luhmann, J.G., Schrijver, C.J., Li, Y.: 2004, Stream structure and coronal sources of the solar wind during the May 12th, 1997 CME, *J. Atmos. Solar-Terr. Phys.* **66**, 1295-1309, doi: 10.1010/j.jastp.2004.03.018.

Detman, T. R., Dryer, M., Yeh, T., Han, S.M., Wu, S.T.: 1991, A time-dependent, three-dimensional MHD numerical study of interplanetary magnetic draping around plasmoids in the solar wind, *J. Geophys. Res.*, ***96*****,** 9531-9540, doi: 10.1029/91JA00443.

Detman, T., Z. Smith, M. Dryer, C. D. Fry, C. N. Arge, V. Pizzo, A hybrid heliospheric modeling system: Background solar wind, *J. Geophys. Res*. **11,** doi: 10.1029/2005JA011430, 2006.

Dryer, M., Interplanetary Studies: Propagation of Disturbances between the sun and the magnetosphere, space Sci. rev. 67, 369-419, doi: 10.1007/BF00756075, 1994.

Dryer, M.; Wu, C.-C.; Smith, Z. K., Three-dimensional MHD simulation of the April 14, 1994, interplanetary coronal mass ejection and its propagation to Earth and Ulysses, *J. Geophys. Res*. **102**, 14065-14074, doi: 10.1029/97JA00872, 1997.

Fry, C. D., Sun, W., Deehr, C. S., Dryer, M., Smith, Z., Akasofu, S.-I., Tokumaru, M. Kojima, M.: 2001, Improvements to the HAF solar wind model for space weather predictions, *J.*

Geophys. Res. ***106***(A10), 20985-21002, DOI: 10.1029/2000JA000220.

Gopalswamy, N. A. Lara, R. P. Lepping, M. L. Kaiser, D.B. Berdichevsky and O. C. St. Cyr, Interplanetary acceleration of coronal mass ejections, *Geophys. Res. Lett.* **27**, 145-148, DOI: 10.1029/1999GL003639, 2000.

Gopalswamy, N., P. Makela, H. Xie, S. Akiyama, and S. Yashiro, CME interactions with coronal holes and their interplanetary consequences, J. Geophys. Res. 114, A00A22, doi: 10.1029/2008JA013686, 2009.

Gosling, J.T., E. Hilder, R.M. MacQueen, R.H. Munro, A.I. Poland, C.L. Ross, Direct observations of a flare related coronal and solar wind disturbance, *Solar Physics* **40**, 439-448, 1975.

Groth, C.P., De Zeeuw, D.L., Gombosi, T.I., Powell, K.G.: 2000, Global three-dimensional MHD simulation of a space weather event: CME formation, interplanetary propagation, and interaction with the magnetosphere, *J. Geophys. Res.* **105**, 25053-25078, doi: 10.1029/2000JA900093.

Han, S. M., A numerical study of two dimensional time-dependent magnetohydrodynamic flows. In: *Ph.D. Thesis*, University of Alabama in Huntsville, 1977.

Han, S. M., S. T. Wu, and M. Dryer, A three-dimensional, time-dependent numerical modeling of super-sonic, super-Alfvénic MHD flow, *Computers and Fluids*, ***16*****,** 81-103, 1988.

Hayashi, K., M. Tokumaru, K. Fujiki, and M. Kojima (2011), Three-dimensional solar wind structures obtained with MHD simulation model using observation-based time-varying inner boundary map paper presented at 10th ASP Conference, *Astron. Soc. of the Pac*., Kaanapali, Hawaii, 13–18 March, 2011.

Hess, P., and R.C. Colaninno, Comparing Automatic CME Detections in Multiple LASCO and

SECCHI Catalogs, *J. Astrophys.* **836**, 134, 10.3847/1538-4357/aa5b85, 2017.

Huttunen, K.E.J., R. Schwenn, V. Bothmer, H.E.J. Koskinen, Properties and geoeffectiveness of magnetic clouds in the rising, maximum and early declining phases of solar cycle 23, *Ann. Geophys.* **23**, 625-641., doi: 10.5194/anngeo-23-625-2005, 2005.

Lax, P. D., and B. Wendroff, Systems of conservation laws, *Comm. Pure. and Appl. Math*. ***13*****,** 217–237, 1960.

Lepping, R. P., C.-C. Wu, and D. B. Berdichevsky, and Szabo, A., Wind Magnetic Clouds for 2010 - 2012: Model Parameter Fittings, Associated Shock Waves, and Comparisons to Earlier Periods, *Solar Phys*. **290**, pp.2265-2290, doi: 10.1007/s11207-015-0755-3, 2015.

Liou, K., C.-C. Wu, M. Dryer, S.-T. Wu, N. Rich, S. Plunkett, L. Simpson, C.D. Fry, K. Schenk, Global simulation of extremely fast coronal mass ejection on 23 July 2012, *J. Atmospheric and Solar-Terrestrial Physics* **121**, 32-41, doi: 10.1016/j.jastp.2014.09.013, 2014.

Lugaz, N., I. I. Roussev, Numerical modeling of interplanetary coronal mass ejections and comparison with heliospheric images, *Journal of Atmospheric and Solar-Terrestrial Physics* **73**, Issue 10, p. 1187-1200, doi: 10.1016/j.jastp.2010.08.016, 2011.

Manchester, W. B., T. I. Gombosi, I. Roussev, A. Ridley, D. D. Zeeuw, I. V. Sokolov, K. G. Powell, and G. Toth, Modeling a space weather event from the Sun to the Earth: CME generation and interplanetary propagation, *J. Geophys. Res.* **109**, A02107, doi:10.1029/2003JA010150, 2004.

Odstrcil, D., and V. J. Pizzo (1999a), Three-dimensional propagation of coronal mass ejections (CMEs) in a structured solar wind flow: 1. CME launched within the streamer belt, *J. Geophys. Res*. **104**, 483–492.

Odstrcil, D., and V. J. Pizzo (1999b), Distortion of interplanetary magnetic field by three-dimensional propagation of CMEs in a structured solar wind, *J. Geophys. Res*. **104**, 28225-28239.

Odstrcil, D., V. J. Pizzo, C. N. Arge, Propagation of the 12 May 1997 interplanetary coronal mass ejection in evolving solar wind structures, *J. Geophys. Res.* **110**, A02106, doi: 10.1029/2004JA010745, 2005.

Sheeley, N.R., Jr., R.A. Howard, M.J. Koomen, D.J. Michels, J.W. Harvey, K.L. Harvey, Observations of coronal structure during sunspot maximum, *Space Sce. Rev.* **33**, 219-231, doi: 10.1007/BF00213255, 1982.

Shen, F., X.S. Feng, S. T. Wu, C.Q. Xiang, W.B. Song, Three-dimensional MHD simulation of the evolution of the April 2000 CME event and its induced shocks using a magnetized plasma blob model, *J. Geophys. Res*. **116,** A04102, doi:10.1029/2010JA015809, 2011.

Usmanov, A. V., A global numerical 3-D MHD model of the solar wind, Solar Physics (ISSN 0038-0938), vol. **146**, no. 2, p. 377-396, doi: 10.1007/BF00662021, 1993.

Vandas, M.; OdstrčIl, D.; Watari, S., Three-dimensional MHD simulation of a loop-like magnetic cloud in the solar wind, *J. Geophys. Res*. **107**, Issue A9, pp. SSH 2-1, CiteID 1236, DOI 10.1029/2001JA005068, 2002.

Vourlidas, A., L.A. Balmaceda, G. Stenborg, and A. Dal Largo, Multi-viewpoint coronal mass ejection catalog based on STEREO COR2 observations, *J. Astrophys.* **838**, 141, doi: 10.3847/1538-4357/aa67f0, 2017.

Wang, C., C.X. Li, Z. H. Huang, and J. D. Richardson, Effect of interplanetary shock strengths and orientations on storm sudden commencement rise times, *Geophys. Res. Lett.* **33**, L14104, doi: 10.1029/2006GL025966, 2006.

Wang, Y.-M, N. R. Sheeley Jr.: 1990, Solar wind speed and coronal flux-tube expansion, *Astrophys. J.* **355***,* 726-732, doi: 10.1086/168805.

Wang, Y.-M, Sheeley Jr., N.R., Nash, A.G.: 1990, Latitudinal distribution of solar wind speed from magnetic observations of the Sun, *Nature* **347**, 439-444, doi: 10.1038/347439a0.

Wang, Y.-M, N. R. Sheeley Jr., On potential field models of the solar corona, *Astrophysical Journal*, Part 1 (ISSN 0004-637X), **392**, 1992, p. 310-319, doi: 10.1086/171430, 1992.

Wang, Y.-M., and R. Colaninno, Is solar cycle 24 producing more coronal mass ejections than cycle 23?, *Astrophys Lett.* **784**, L27, doi: 10.1088/2041-8205/784/2/L27, 2014.

Webb, D, R. P. Lepping, L. F. Burlaga, C.E. DeForest, D. E. Larson, S. F. Martin, S. P. Plunkett, D. M. Rust, The origin and development of the May 1997 magnetic cloud, *J. Geophys. Phys.* Volume **105**, Issue A12, p. 27251-27260, 2000.

Wood, B.E., C.-C. Wu, R. A. Howard, D. G. Socker, A. P. Rouillard, Empirical Reconstruction and Numerical Modeling of the First Geoeffective Coronal Mass Ejection of Solar Cycle 24, *Astrophysical J.,* **729**:70, 10.1088/0004-637X/729/1/70, 2011.

Wood, B. E., C.-C. Wu, A. P. Rouillard, R. A. Howard, D. G. Socker, A Coronal Holes's Effects on CME Shock Morphology in the Inner Heliosphere, *Astrophysical J.* **755**, article id. 43, doi:10.1088/0004-637X/755/1/43, 2012.

Wu, C.-C. and R. P. Lepping, Effects of Magnetic Clouds on the Occurrence of Geomagnetic Storms: The First 4 Years of Wind, J. Geophysics Res., 107(A10), 1314, doi:10.1029/2001JA000161, 2002.

Wu, C.-C. and R. P. Lepping, Comparison of the characteristics of magnetic clouds and magnetic cloud-like structures for the events of 1995-2003, Solar Physics., 242, 159-165, DOI 10.1007/s11207-007-0323-6, 2007.

Wu, C. C.; Lepping, R. P.; Comparisons of Characteristics of Magnetic Clouds and Cloud-Like

Structures During 1995-2012, *Solar Physics*, **290**, pp. 1243-1269, doi: 10.1007/s11207-015-0656-5, 2015.

Wu, Chin-Chun, Murray Dryer, and S. T. Wu, Three-dimensional MHD simulation of interplanetary magnetic field changes at 1 AU as a consequence of simulated solar flares, *Ann. Geophys.* **14**, 383-399, doi: 10.1007/s00585-996-0383-1, 1996.

Wu, Chin-Chun and Murray Dryer, Three-Dimensional MHD Simulation of Interplanetary Magnetic Field Changes at 1 AU Caused by a Simulated Solar Disturbance and a Tilted Heliospheric Current/plasma Sheet, *Solar Physics*, **173**, 391-408, 1997.

Wu, Chin-Chun, C.D. Fry, D. B. Berdichevsky, M. Dryer, Z. Smith, T. Detman, Predicting the Arrival Time of Shock Passages at Earth, *Solar Physics*, **227**, 371-386, doi: 10.1007/s11207-005-1213-4, 2005.

Wu, C. C.; Lepping, R. P.; Gopalswamy, N., Relationships Among Magnetic Clouds, CMES, and Geomagnetic Storms, *Solar Physics*, **239**, pp. 449-460, doi: 10.1007/s11207-006-0037-1, 2006.

Wu, Chin-Chun, X. S. Feng, S. T. Wu, M. Dryer, C. D. Fry, Effects of the interaction and evolution of interplanetary shocks on "background" solar wind speeds, *J. Geophys. Res.,* **111**, A12104, doi:10.1029/2006JA011615, 2006.

Wu, Chin-Chun, C. D. Fry, S. T. Wu, M. Dryer, and K. Liou, Three-dimensional global simulation of ICME propagation from the Sun to the heliosphere: 12 May 1997 solar event, *J. Geophys. Res*., **112**, A09104, DOI:10.1029/2006JA012211, 2007a.

Wu, Chin-Chun, C. D. Fry, S. T. Wu, M. Dryer, Barbara Thompson, Kan Liou, and X. S. Feng, Three-dimensional global simulation of multiple ICMEs' interaction and propagation from the Sun to the heliosphere following the 25-28 October 2003 solar events, coronal mass ejections, *Adv. Space Rev.*, **40**, 1827-1834, doi:10.1016/j.asr.2007.06.025, 2007b.

Wu, Chin-Chun, Murray Dryer, S. T. Wu, Brian Wood, C. D. Fry, Kan Liou, and Simon Plunkett, Global Three-dimensional simulation of the interplanetary evolution of the observed geoeffective CME during the epoch August 1-4, 2010, *J. Geohys. Res.* **116**, A12103, 13 PP., doi:10.1029/2011JA016947, 2011.

Wu, C.-C., S. T. Wu, K. Liou, and S. Plunkett, Evolution of a Magnetohydrodynamic Coronal Shock, AIP Conf. Proc. 1500, pp. 50-55; doi:http://dx.doi.org/10.1063/1.4768744 (6 pages) SPACE WEATHER: THE SPACE RADIATION ENVIRONMENT: 11th Annual International Astrophysics Conference Date: 19-23 March 2012.

Wu, Chin-Chun, Kan Liou, Angelos Vourlidas, Simon Plunkett, Murray Dryer, S. T. Wu, and Richard A. Mewald, Global Magnetohydrodynamic simulation of the March 15, 2013 Coronal Mass Ejection Event – Interpretation of the 30-80 MeV Proton Flux, *J. Geophys. Res.* **121**, doi:10.1002/2015JA021051, 2016a.

Wu, Chin-Chun, Kan Liou, Angelos Vourlidas, Simon Plunkett, Murray Dryer, S. T. Wu, Dennis Socker, Brian E. Wood, Lynn Hutting, and R. Howard, Numerical Simulation of Multiple CME-Driven Shocks in the Month of 2011 September, *J. Geophys. Res.* **121**, doi: 10.1002/2015JA021843, 2016b.

Wu, C.-C., Liou, K., Lepping, R.P., Hutting, L.: 2019, The 04-10 September 2017 Sun-Earth connection events: solar flares, coronal mass ejections/magnetic clouds, and geomagnetic storms, *Solar Phys.* **294**:110, DOI. 10.1007/s11207-019-1446-2.

Wu, S.T., C.-C. Wu, K. Liou, S. Plunkett, M. Dryer, and C.D. Fry, Analyses of the Evolution and Interaction of Multiple Coronal Mass Ejections and Their Shocks in July 2012, *Outstanding Problems in Heliophysics: From Coronal Heating to the Edge of the*

Heliosphere. Proceedings of a conference held 14-19 April 2013 at Myrtle Beach, South Carolina, USA. Edited by Qiang Hu and G.P. Zank. ASP Conference Series, **484**, p.241, 2014.

Yu, H.-S., B. V. Jackson, P.P. Hick, A. Buffington, D. Odstrcil, C.-C. Wu, J.A. Davies, M. M. Bisi, M. Tokumaru, 3D Reconstruction of Interplanetary Scintillation (IPS) Remote-Sensing Data: Global Solar Wind Boundaries for Driving 3D-MHD Models, *Solar Physics*, Volume 290, Issue 9, pp.2519-2538, 2015.

Zhang, J., I.G. Richardson, D. F. Webb, N. Gopalswamy, E. Huttunen, J. Kasper, N. Nitta, W. Poomvises, B. J. Thompson, C.-C. Wu, S. Yashiro, and Z. Zhukov, Solar and Interplanetary Sources of Major Geomagnetic Storms (Dst < - 100 nT) during 1996 - 2005, *J. Geophys. Res*. **112**, A10102, doi:10.1029/2007JA012321, 2007.

Figure Captions

Figure 1. Background (corotating "steady state") solar wind condition in the plane at (a,c) 18 and (b,d) 216 R_s on 4 April 2009, 15:00UT by using velocity formula, $Vr = 150 + 250 f_s^{-0.4}$ (Fig. 1a-b), and $Vr = 150 + 500 f_s^{-0.4}$ (Fig. 1c-d).

Figure 2. Velocity profile at the solar-equatorial plane using velocity formula, $Vr = 150 + 300 f_s^{-0.4}$ for velocity variation at 18 R_s. It takes about 6 days to get a settle down background solar wind (See Fig.2f).

Figure 3. Solar wind speed (a-d) and density (e-h) on surfaces of different angular cones that are centered at the Sun's center. These conical angles are at 22.5ºN (north, representative of a response in the northern heliosphere), 7.5ºN, 7.5ºS (close to Earth's latitude in the solar equatorial coordinate system), 22.5ºS (south, representative of a response in the southern heliosphere). Figures 3i-3m show the solar wind speed at different longitudinal meridian plane: 90ºE (East, Fig.3i), 45ºE (Fig.3j), 0ºW (west, 3k), 45ºW (Fig.3l), 90ºW (Fig.3m).

Figure 4.
Figure 4. Variation of solar wind speed at L_1 during March-April 2009. Red-dotted and Black-solid lines represent observation (OMNI) and H3DMHD simulation results. Solar wind speed was constructed by using speed formula, $V_{18Rs} = V_1 + V_2 f_s^{-0.4}$ (km/s). V_1 ranges between 150 and 350 (panels 1-9: $V_1$was 150,175, 200, 225, 250, 275, 300, 325, and 350, respectively). V_2 ranges between 250 to 500 (left to right panels A-F: V_2 was 250, 300, 350, 400, 450, and 500, respectively). f_s is the expansion factor which was derived by using Wang and Sheeley model [1990].

Figure 5. Correlation coefficients for different V_os' (ranges between 150 and 350) and V_1s' (ranges between 250 and 500) for CR2082. Colors and red-contours : Correlation coefficient x 100 (%). Light-blue-contours: differences between $<V_{obs.}>$ and $<V_{H3DMHD}> = (<V_{H3DMHD}> - <V_{obs}>)/<V_{obs.}>$ x 100 (%) .

Figure 6. Comparison of the simulated background solar wind for H3DMHD (black-solid-lines, at S2.5º) vs. observation (*OMNI* in red-dotted-lines). (a) $Vr =150+250 f_s^{-0.4}$ was used to construct solar wind speed at 18 R_s. (b) $Vr =150+500 f_s^{-0.4}$" was used to construct solar wind speed at 18 R_s.

Figure 7. Examining the expansion factor (f_s) on the Vr profile for 2082 with different power law of expansion factor: (a) $Vr = 150 + 500 f_s^{-0.1}$; (b) $Vr = 150 + 500 f_s^{-0.2}$; (c) $Vr = 150 + 500 f_s^{-0.4}$; (d) $Vr = 150 + 500 f_s^{-0.6}$. Solid-lines: H3DMHD results. Dotted-lines: observation.

Figure 8. Comparison of solar wind speed, density, temperature, and temperature from the *WIND* spacecraft (red-dotted lines) with WS-H3DMHD prediction (black solid lines) for CR1899 (during 6 August - 2 September 1995). A data gap of *WIND* was marked between two blue vertical dotted lines.

Figure 9. Comparison of the full rotation solar wind speed predictions (solid black lines) with 1-hours-averaged WIND satellite velocity observation (red dotted lines) for Carrington rotation 1921, 1922, and 1923.

Figure 10. Comparison of solar wind speed, density, temperature, and temperature from the *WIND* spacecraft (red-dotted lines) with WS-H3DMHD prediction (black solid lines) during September-October 2017 without adding simulated CME perturbation (left panel), and during 04-11 September 2017 with two CMEs perturbation on 04-09-2017 and 06-09-2017 (right panel), respectively. Blue vertical dotted lines indicated the interplanetary (IP) shock arrival time at the *WIND* spacecraft. Shock06 and Shock07 represent the IP shock arrived at the *WIND* on the 6th and 7th of September.

Figure 11. Ratio of correlation coefficient [cc] over MAPE for different V_1s (ranges between 150 and 350) and V_2s (ranges between 250 and 500) during 2008 (CR2066-CR2077) using $V = V_1 + V_2 f_s^{-0.4}$. Colors represent the "ratio for the (cc divided by MAPE) × 100 [%]".

Figure A. Variation of solar wind speed at L_1 during 2008. *Red-dotted* and *black-solid* lines represent, respectively, observation (OMNI) and H3DMHD simulation results. Solar wind speed was constructed by using the speed formula, $V_{18Rs} = V_1 + V_2 f_s^{-0.4}$ [km s^{-1}]. V_1 ranges between 150 and 350 km s^{-1} in increments of 25 km s^{-1} (*top to bottom,* panels, **1 – 9**). V_2 ranges between 250 to 500 km s^{-1} in increments of 50 km s^{-1} (*left to right,* panels **A – F**). f_s is the expansion factor that was derived by using Wang and Sheeley model (1990). Correlation coefficient [cc], mean absolute percentage error [$\text{MAPE} \equiv 100/N \times \sum |(V_{Wind} - V_{G3DMHD})/V_{Wind}|$], and standard deviation [σ] are marked on the top of each panel (left to right). For example, for the case on the top-left corner (Case E5): $V_{18Rs} = 250 + 450 f_s^{-0.4}$, values of cc, MAPE, σ, and cc/MAPE are 0.75, 10 %, 59, and 7.1, respectively.

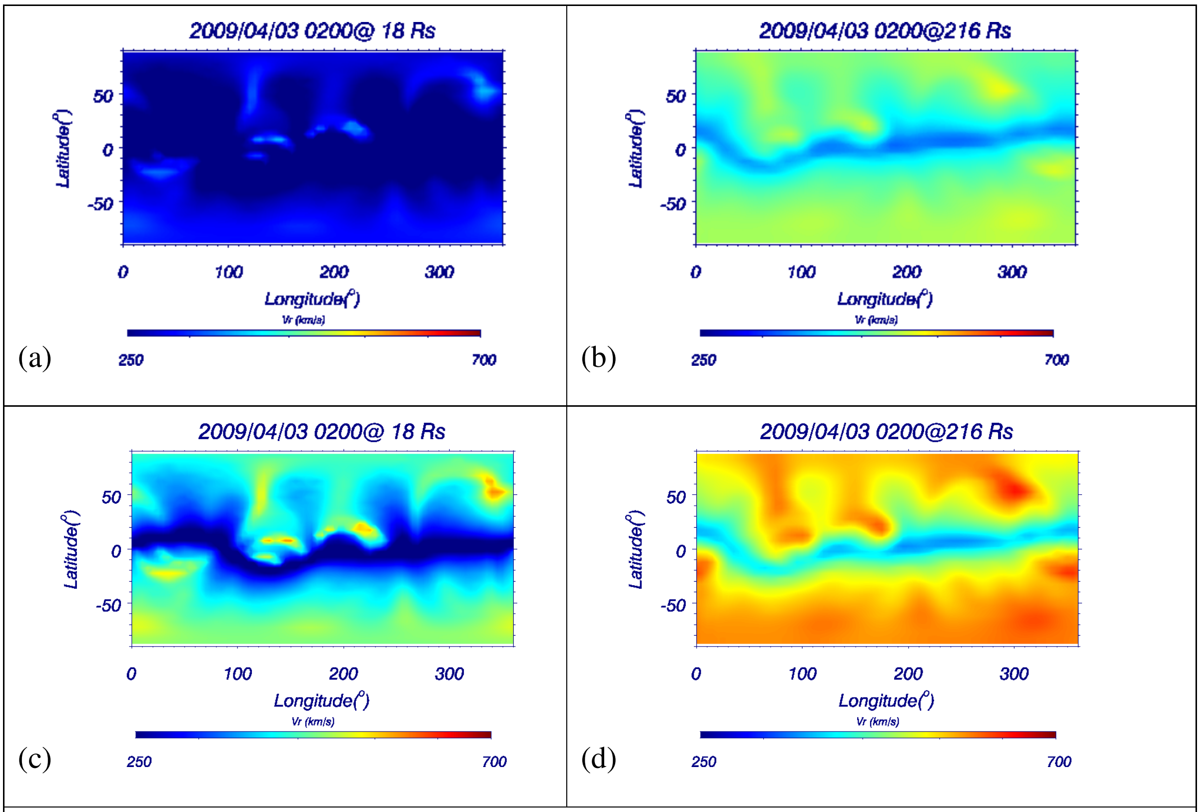

Figure 1. Background (corotating "steady state") solar wind condition in the plane at (a,c) 18 and (b,d) 216 R_s on 4 April 2009, 15:00UT by using velocity formula, Vr = 150 + 250 $f_s^{\ -0.4}$ (Fig. 1a-b), and Vr = 150 + 500 $f_s^{\ -0.4}$ (Fig. 1c-d).

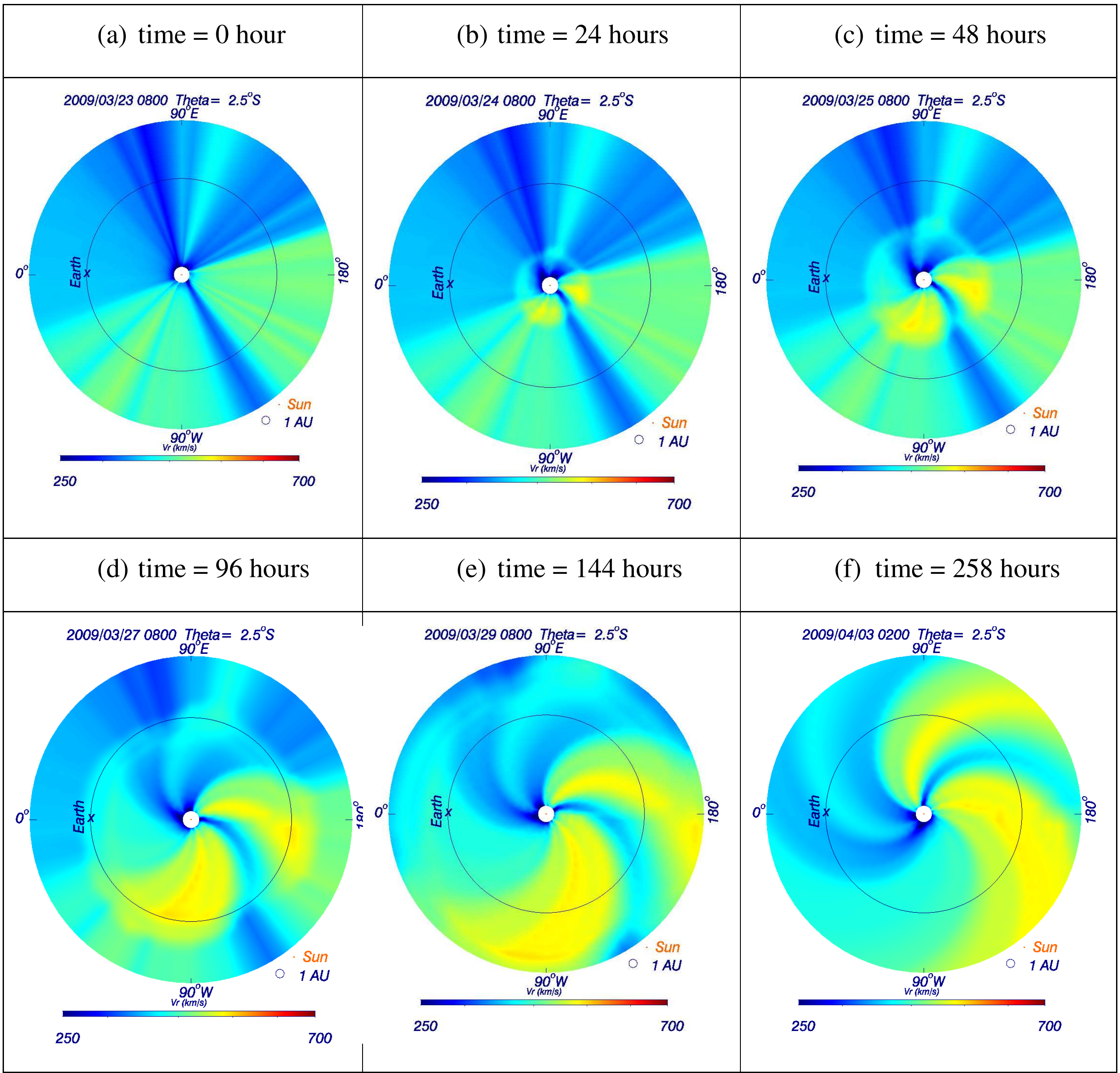

Figure 2. Velocity profile at the solar-equatorial plane using velocity formula, Vr = 150 + 300 $f_s^{-0.4}$ for velocity variation at 18 R_s. It takes about 6 days to get a settle down background solar wind (See Fig.2f).

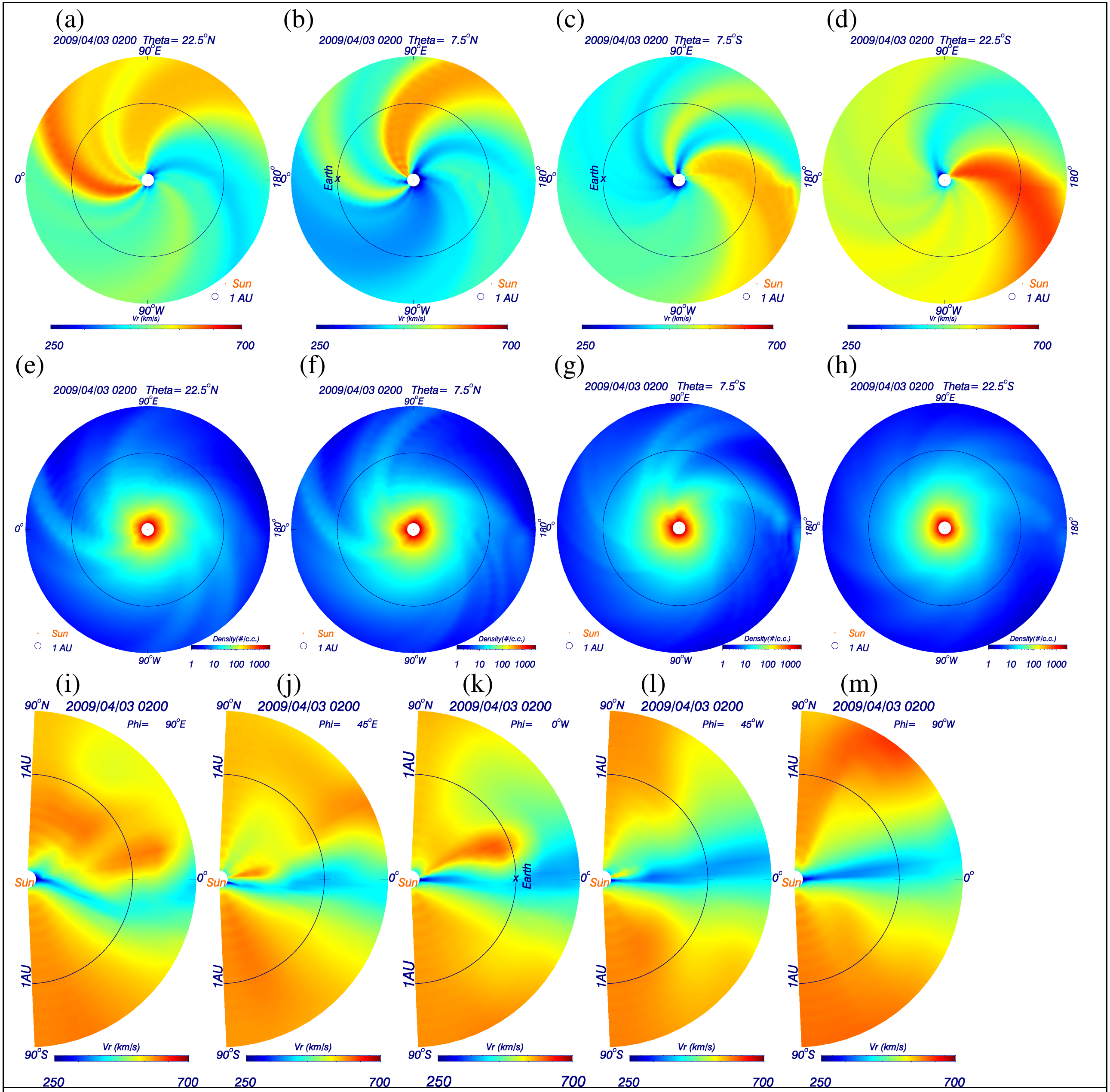

Figure 3. Solar wind speed (a-d) and density (e-h) on surfaces of different angular cones that are centered at the Sun's center. These conical angles are at 22.5ºN (north, representative of a response in the northern heliosphere), 7.5ºN, 7.5ºS (close to Earth's latitude in the solar equatorial coordinate system), 22.5ºS (south, representative of a response in the southern heliosphere). Figures 3i-3m show the solar wind speed at different longitudinal meridian plane: 90ºE (East, Fig.3i), 45ºE (Fig.3j), 0ºW (west, 3k), 45ºW (Fig.3l), 90ºW (Fig.3m).

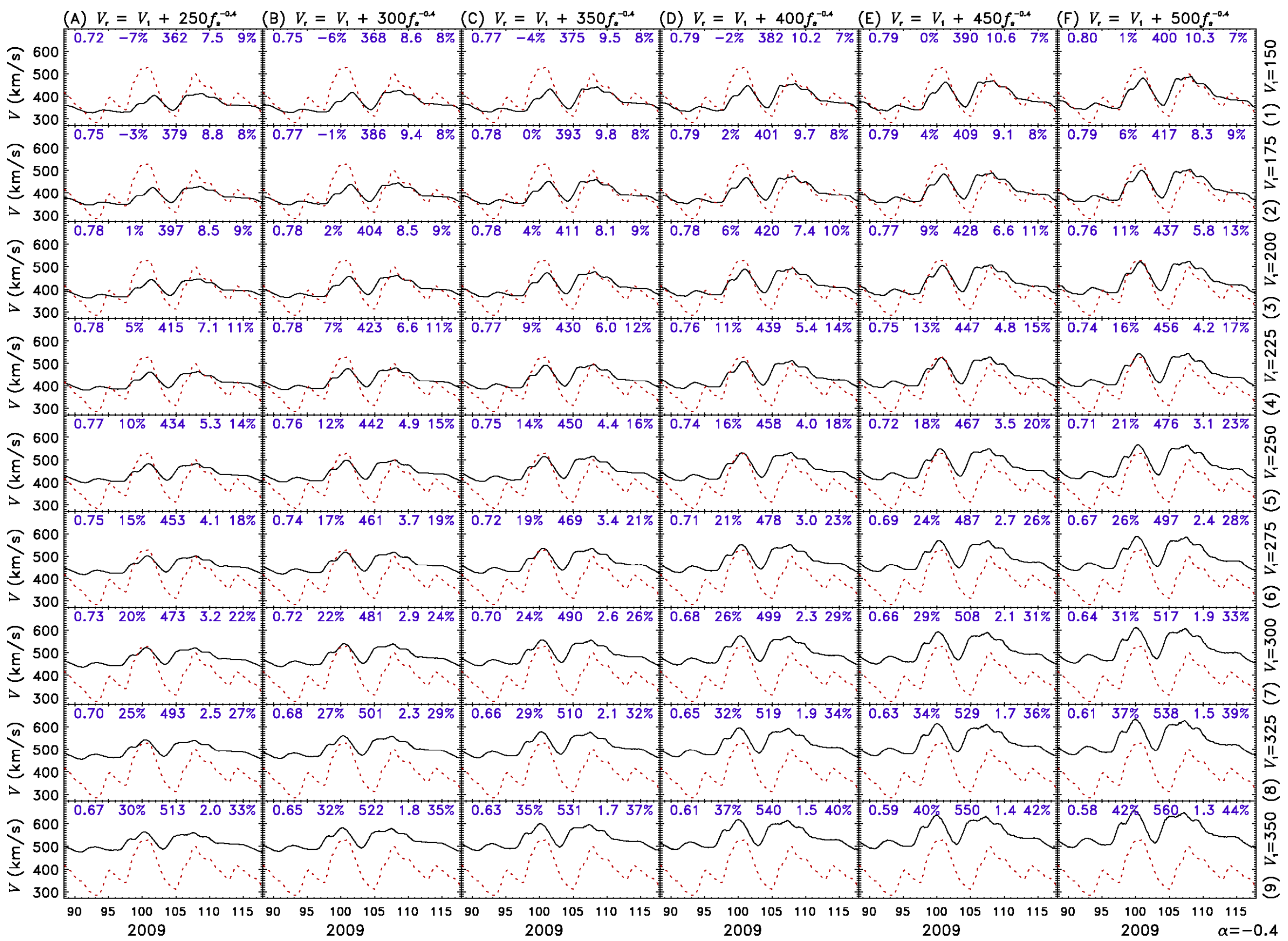

Figure 4. Variation of solar wind speed at L_1 during March – April 2009. *Red-dotted* and *black-solid* lines represent, respectively, observation (OMNI) and H3dMHD simulation results. Solar wind speed was constructed by using the speed formula, $V_{18R_s} = V_1 + V_2 f_s^{-0.4}$ [km s^{-1}]. V_1 ranges between 100 and 350 km s^{-1} in increments of 25 km s^{-1} (*top to bottom,* panels, **1 – 9**). V_2 ranges between 250 to 500 km s^{-1} in increments of 50 km s^{-1} (*left to right,* panels **A – F**). f_s is the expansion factor that was derived by using Wang and Sheeley model (1990). Correlation coefficient [cc], the difference between $\langle V \rangle_{\mathrm{OMNI}}$ and $\langle V \rangle_{\mathrm{3DMHD}}$ (Diff ≡ ($\langle V \rangle_{OMNI}$ - $\langle V \rangle_{\mathrm{3DMHD}}$) / $\langle V \rangle_{\mathrm{OMNI}}$), the average simulated solar wind speeds ($\langle V \rangle_{\mathrm{3DMHD}}$), cc/MAPE, and mean absolute percentage error [MAPE ≡ $100/N \times \sum |(V_{Wind} - V_{\mathrm{G3DMHD}})/V_{Wind}|$] are marked on the top of each panel (left to right). $\langle V \rangle_{OMNI}$ is 393 km s^{-1}.For example, for the case on the top-left corner (Case A1): $V_{18R_s} = 150 + 250 f_s^{-0.4}$, values of cc, Diff, $\langle V \rangle_{\mathrm{3DMHD}}$, cc/MAPE, and MAPE are 0.72, -7 %, 362, 7.5, and 9%, respectively.

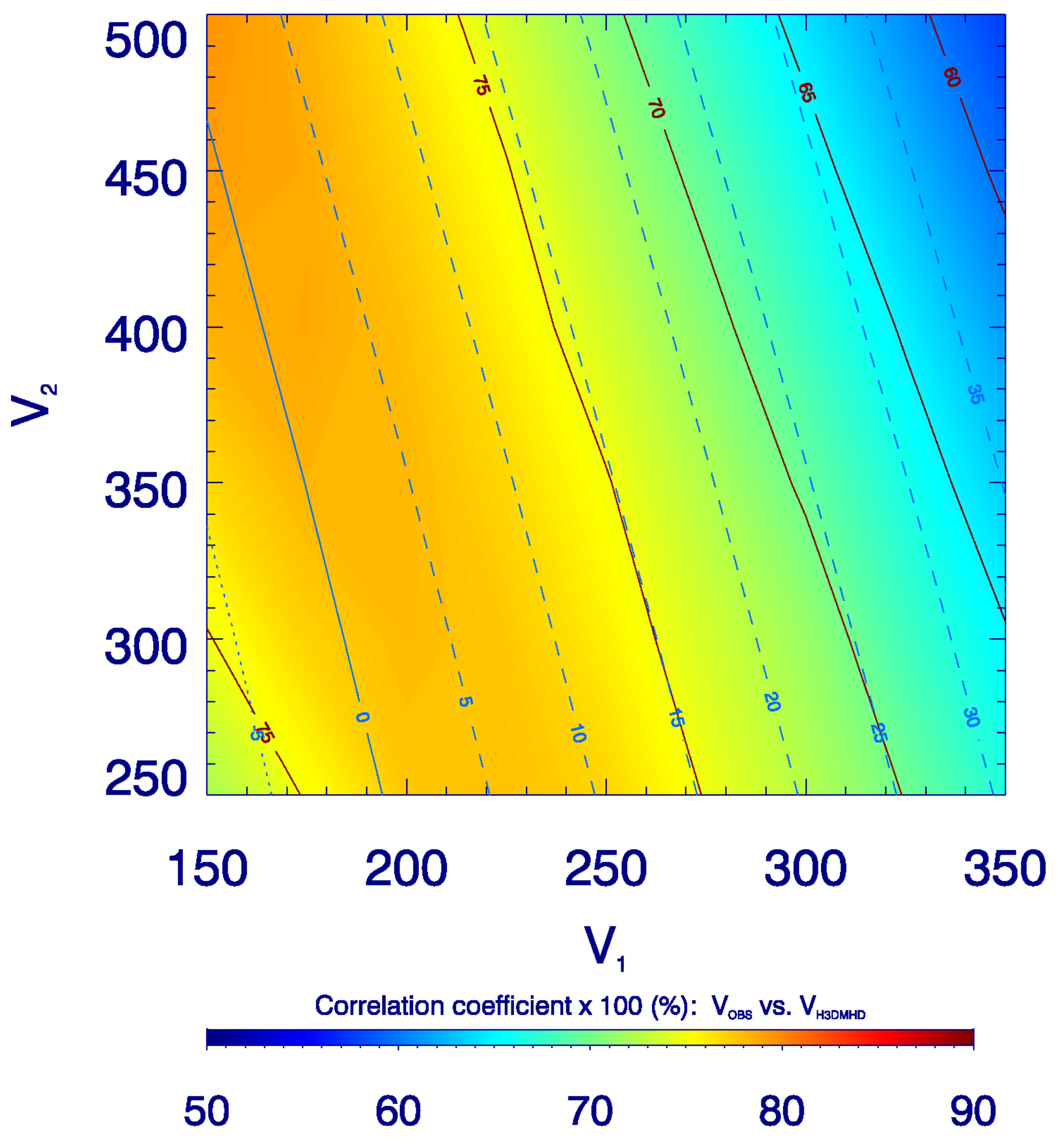

Figure 5. Correlation coefficients for different V_1s' (ranges between 150 and 350) and V_2s' (ranges between 250 and 500) for CR2082. Colors and red-contours : Correlation coefficient x 100 (%). Light-blue-contours: differences between $\langle V_{obs.} \rangle$ and $\langle V_{H3DMHD} \rangle = (\langle V_{H3DMHD} \rangle - \langle V_{obs} \rangle)/\langle V_{obs.} \rangle \times 100$ (%) .

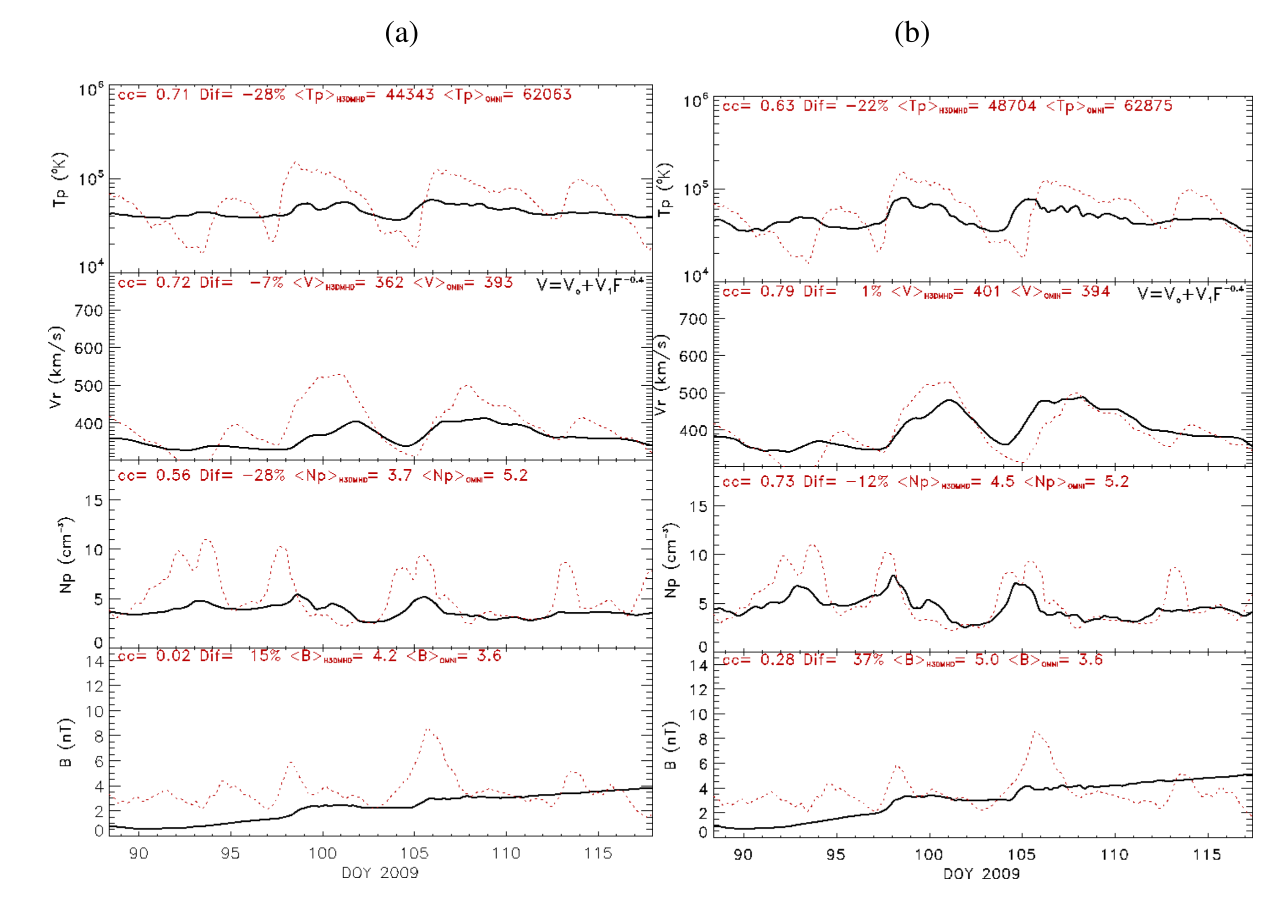

Figure 6. Comparison of the simulated background solar wind for H3DMHD (black-solid-lines, at S2.5°) vs. observation (*OMNI* in red-dotted-lines). (a) Vr=150+250 $f_s^{\ -0.4}$ was used to construct solar wind speed at 18 R_s. (b) Vr=150+500 $f_s^{\ -0.4}$ was used to construct solar wind speed at 18 R_s.

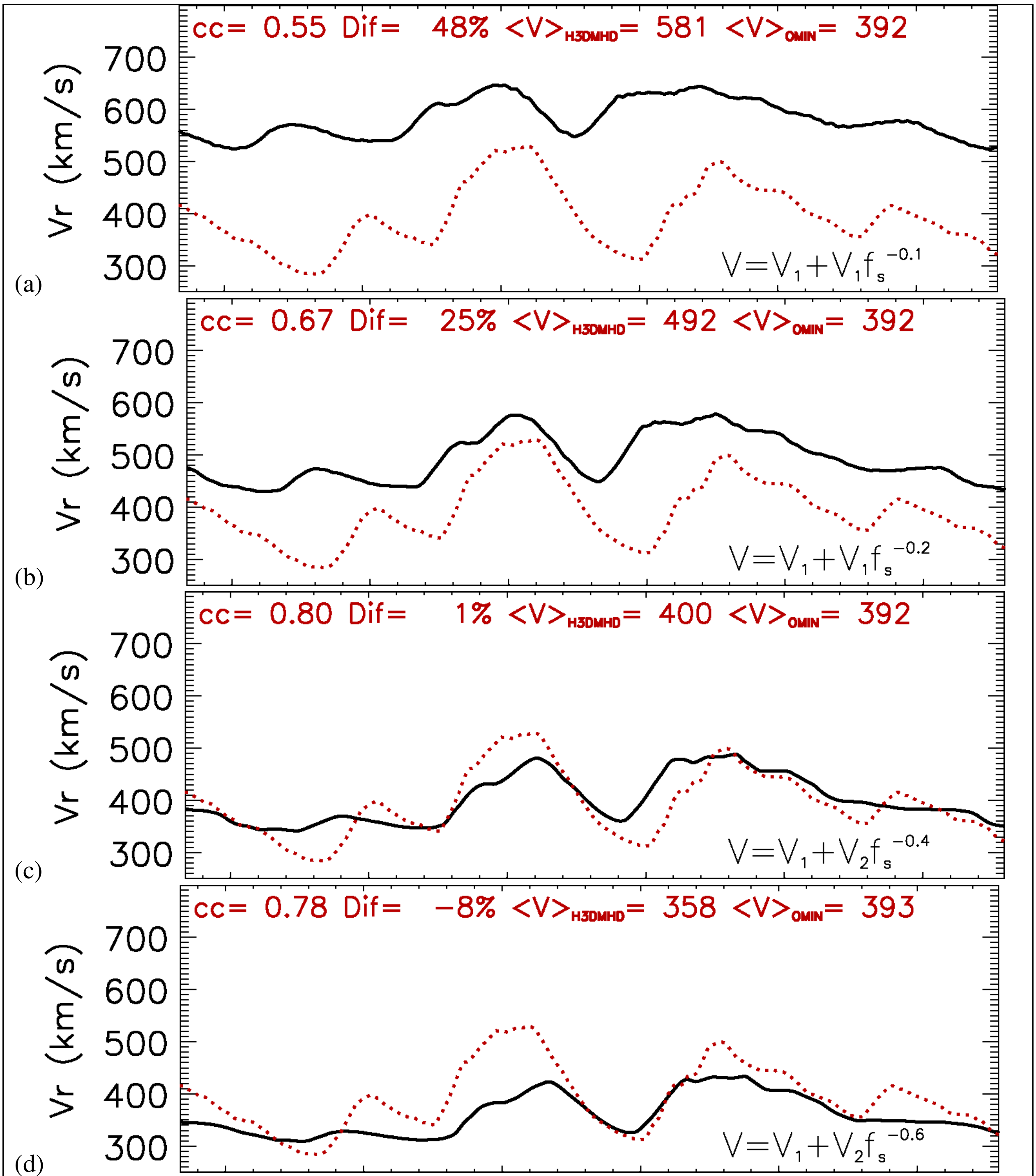

Figure 7. Examining the expansion factor (F) on the *Vr* profile for 2082 with different power law of expansion factor: (a) Vr = 150 + 500 $f_s^{-0.1}$; (b) Vr = 150 + 500 $f_s^{-0.2}$; (c) Vr = 150 + 500 $f_s^{-0.4}$; (d) Vr = 150 + 500 $f_s^{-0.6}$. Solid-lines: H3DMHD results. Dotted-lines: observation.

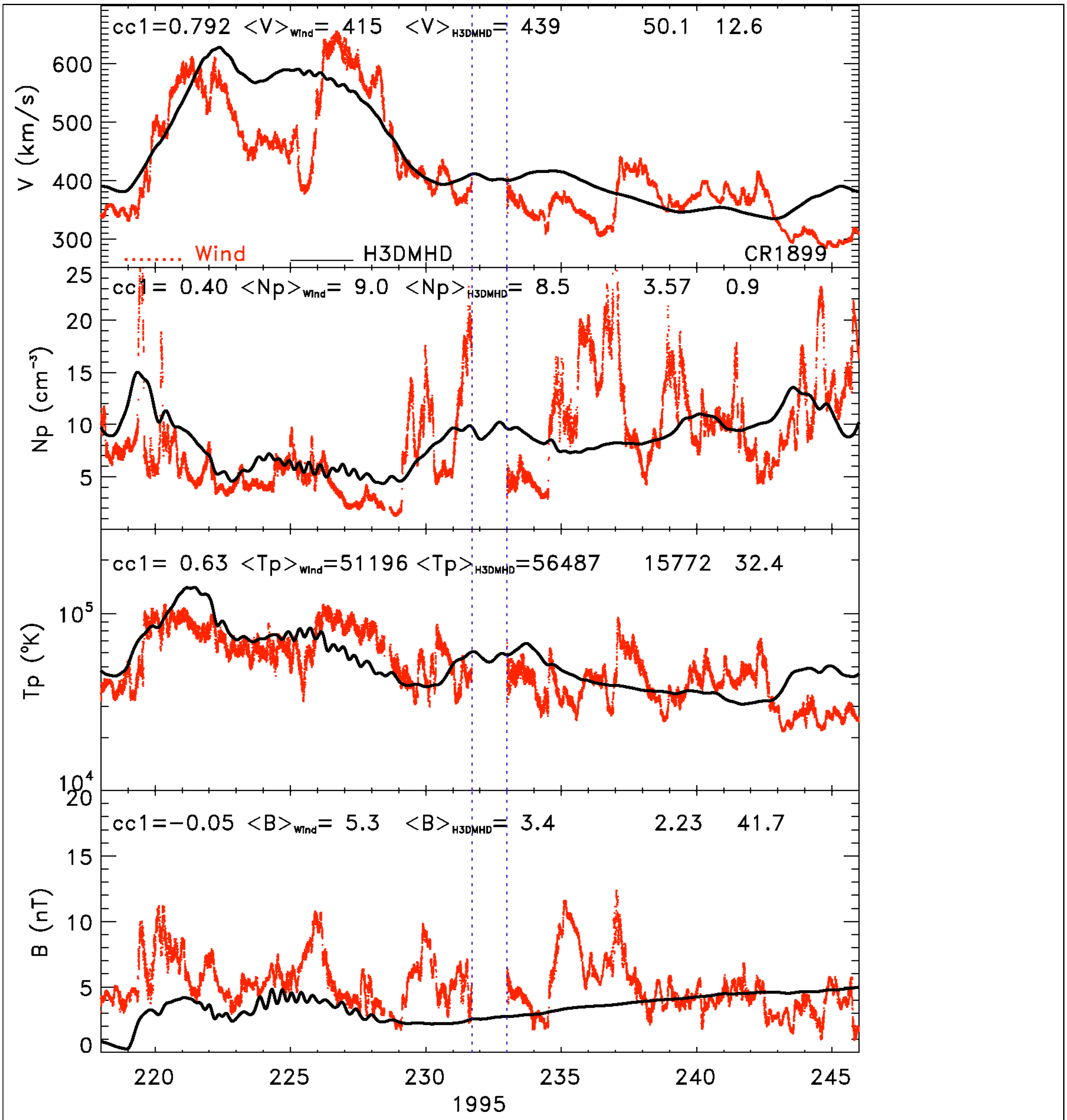

Figure 8. Comparison of solar wind speed, density, temperature, and temperature from the *WIND* spacecraft (red-dotted lines) with WS-H3DMHD prediction (black solid lines) for CR1899 (during 6 August - 2 September 1995). A data gap of *WIND* was marked between two blue vertical dotted lines.

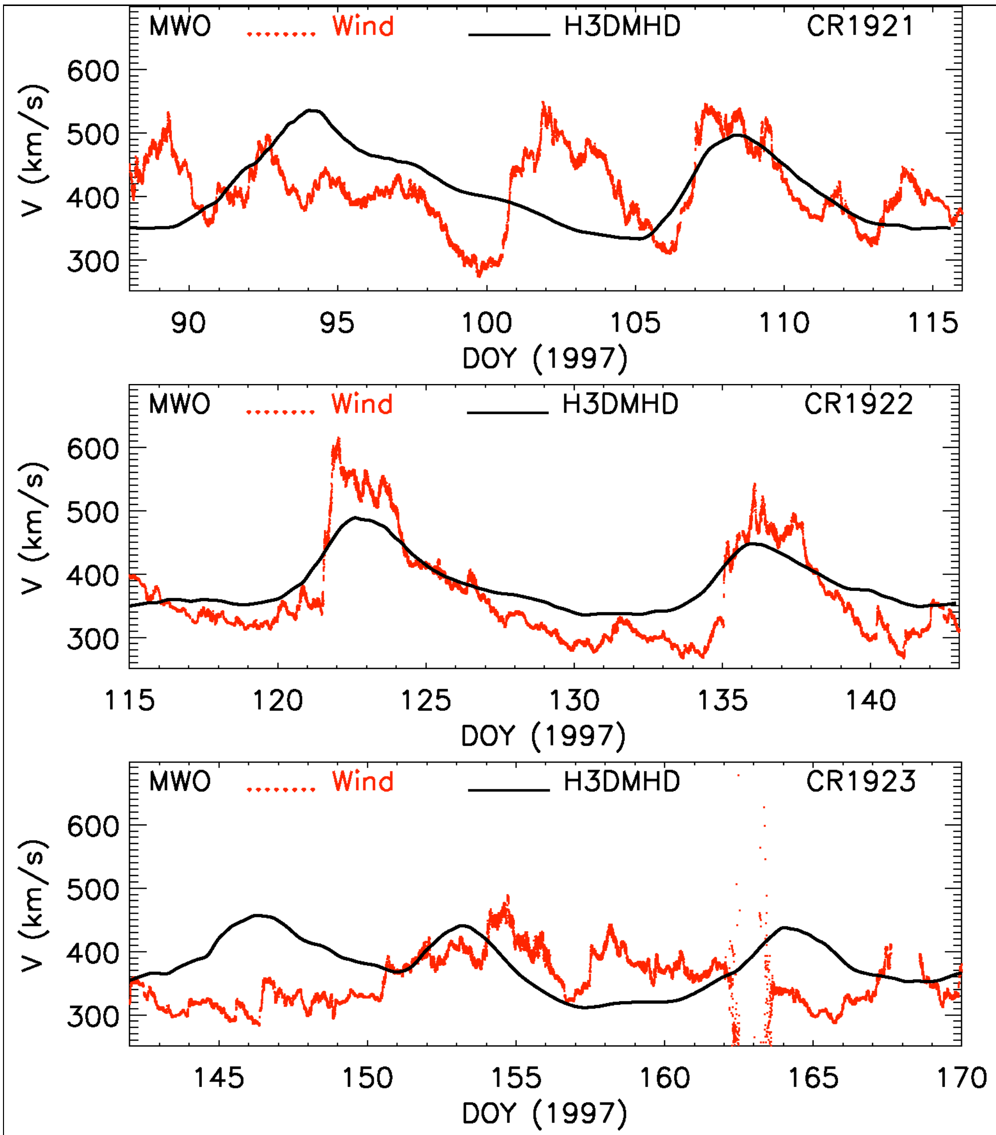

Figure 9. Comparison of the full rotation solar wind speed predictions (solid black lines) with 1-hours-averaged WIND satellite velocity observation (red dotted lines) for Carrington rotation 1921, 1922, and 1923.

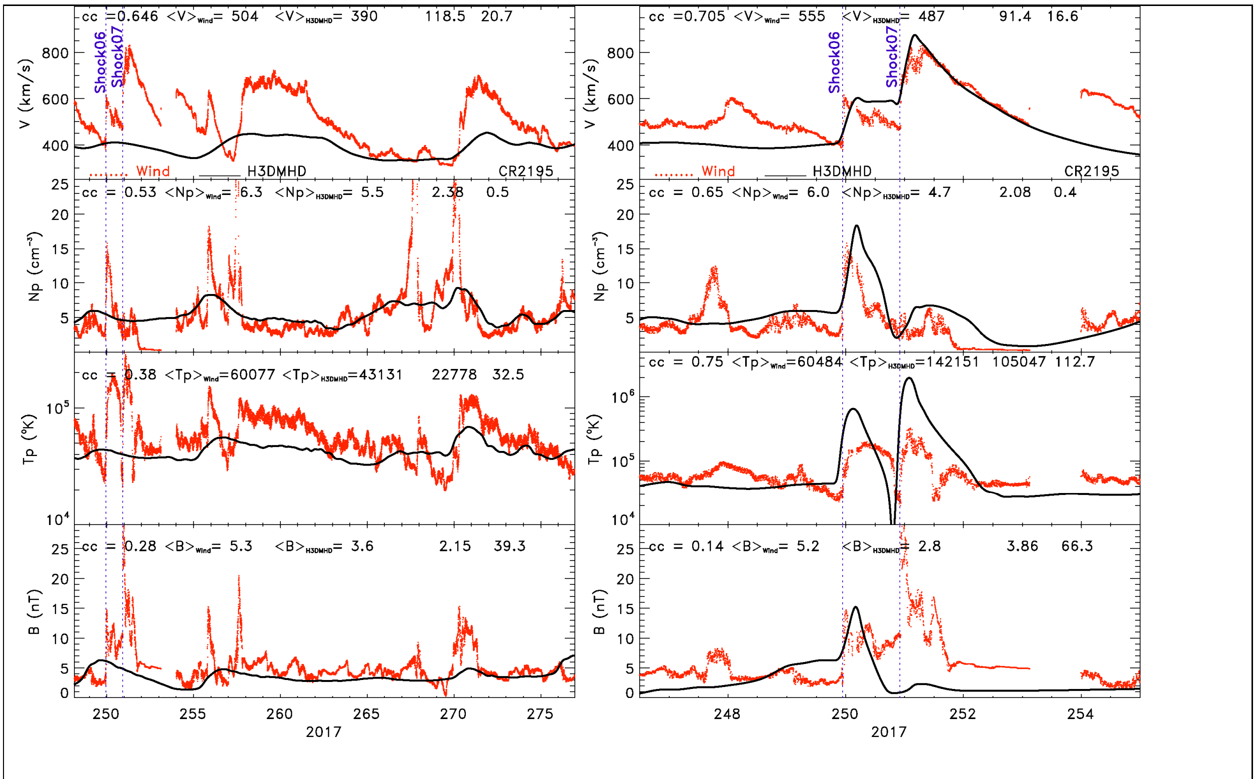

Figure 10. Comparison of solar wind speed, density, temperature, and temperature from the *WIND* spacecraft (red-dotted lines) with WS-H3DMHD prediction (black solid lines) during September-October 2017 without adding simulated CME perturbation (left panel), and during 04-11 September 2017 with two CMEs perturbation on 04-09-2017 and 06-09-2017 (right panel), respectively. Blue vertical dotted lines indicated the interplanetary (IP) shock arrival time at the *WIND* spacecraft. Shock06 and Shock07 represent the IP shock arrived at the *WIND* on the 6th and 7th of September.

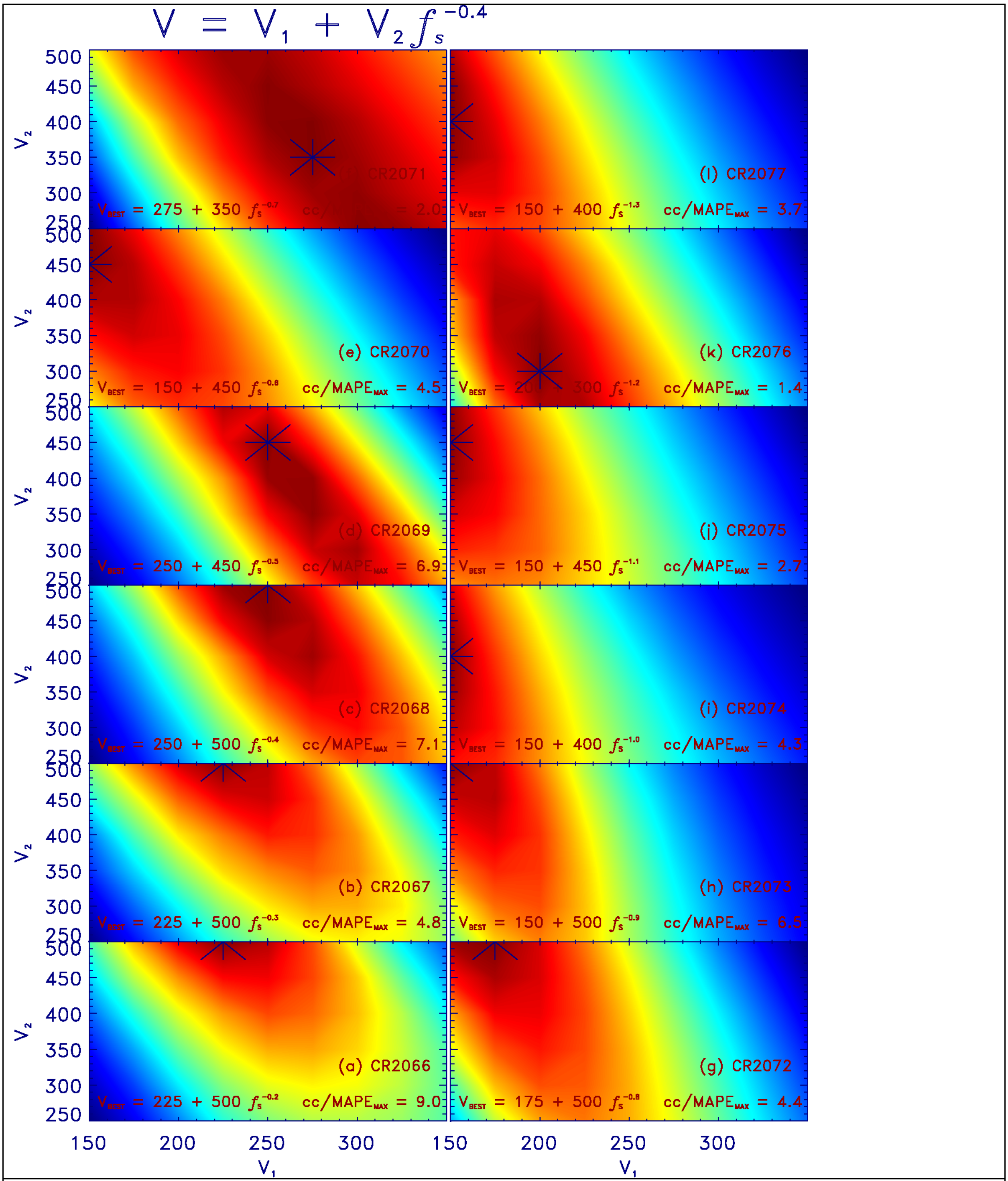

Figure 11. Ratio of correlation coefficient [cc] over MAPE for different V_1s (ranges between 150 and 350) and V_2s (ranges between 250 and 500) during 2008 (CR2066-CR2077) using $V = V_1 + V_2 f_s^{-0.4}$. Colors represent the "ratio for the (cc divided by MAPE) × 100 [%]".

Appendix

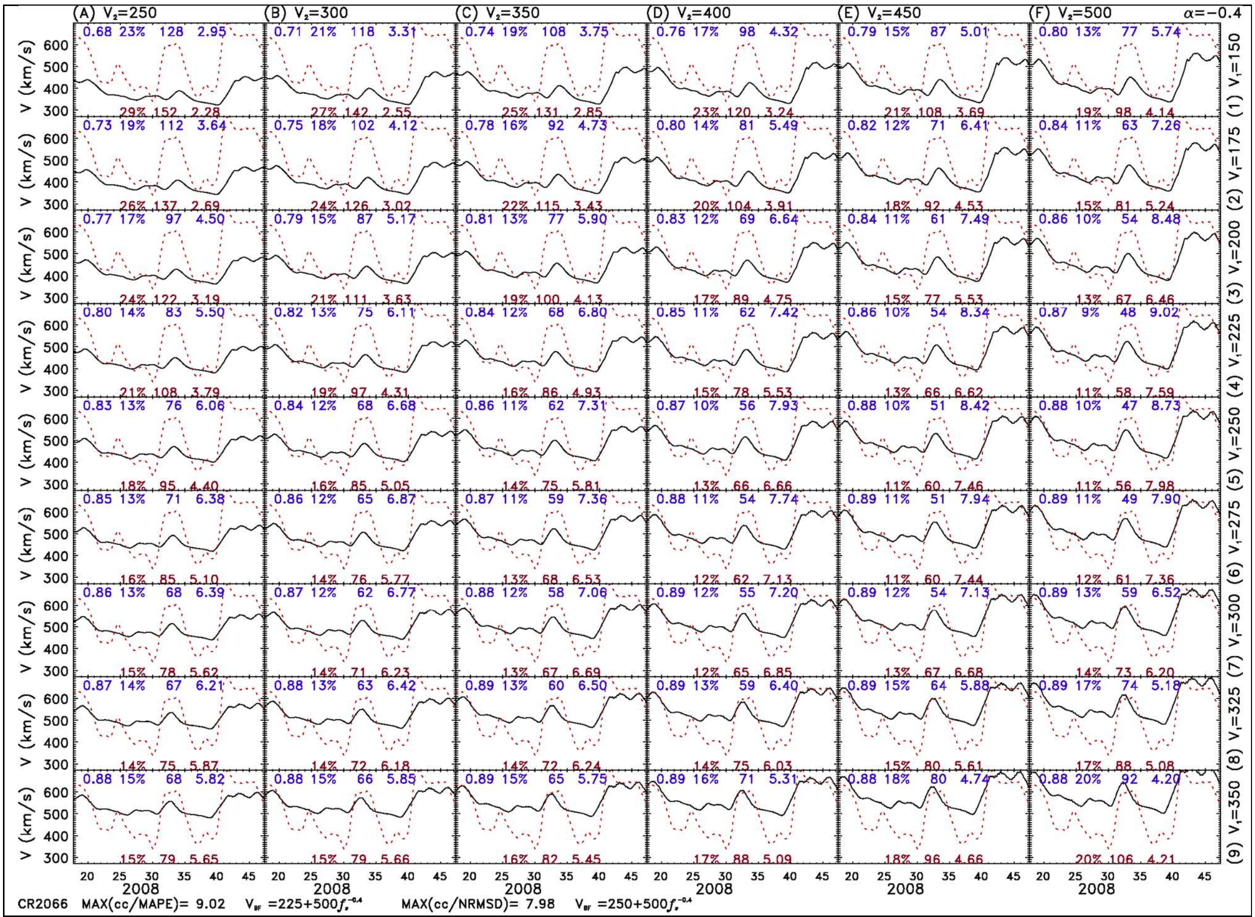

Figure A1. Variation of solar wind speed at L_1 during CR2066 (January – February, 2008). *Red-dotted* and *black-solid* lines represent, respectively, observation (OMNI) and H3DMHD simulation results. Solar wind speed was constructed by using the speed formula, $V_{18Rs} = V_1 + V_2\, f_s^{-0.4}$ [km s^{-1}]. V_1 ranges between 150 and 350 km s^{-1} in increments of 25 km s^{-1} (*top to bottom,* panels, **1 – 9**). V_2 ranges between 250 to 500 km s^{-1} in increments of 50 km s^{-1} (*left to right,* panels **A – F**). f_s is the expansion factor that was derived by using Wang and Sheeley model (1990). Correlation coefficient [cc], mean absolute percentage error [MAPE ≡ 100/*N* x ∑ |(V$_{Wind}$ – V$_{G3DMHD}$)/V$_{Wind}$|], and standard deviation [σ] are marked on the top of each panel (left to right). For example, for the case on the middle-left (Case F4): V_{BF} = 225 + 500 $f_s^{-0.4}$, values of cc, MAPE, σ, and cc/MAPE are 0.87, 9 %, 48, and 9.02, respectively. Values of NRMSD, Root-mean-square deviation (RMSD), and cc/NRMSD are marked on the bottom of each panel (left to right).

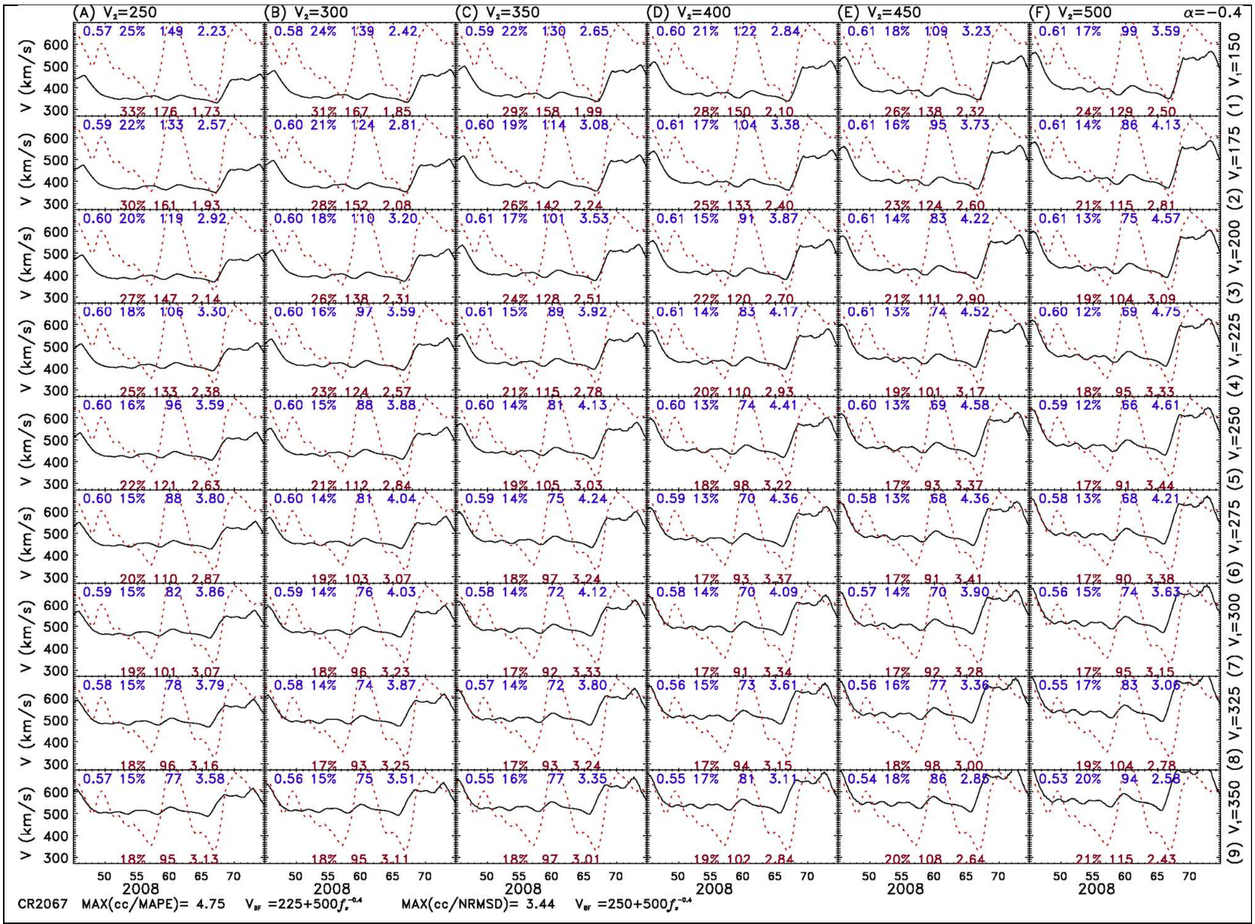

Figure A2. CR2067

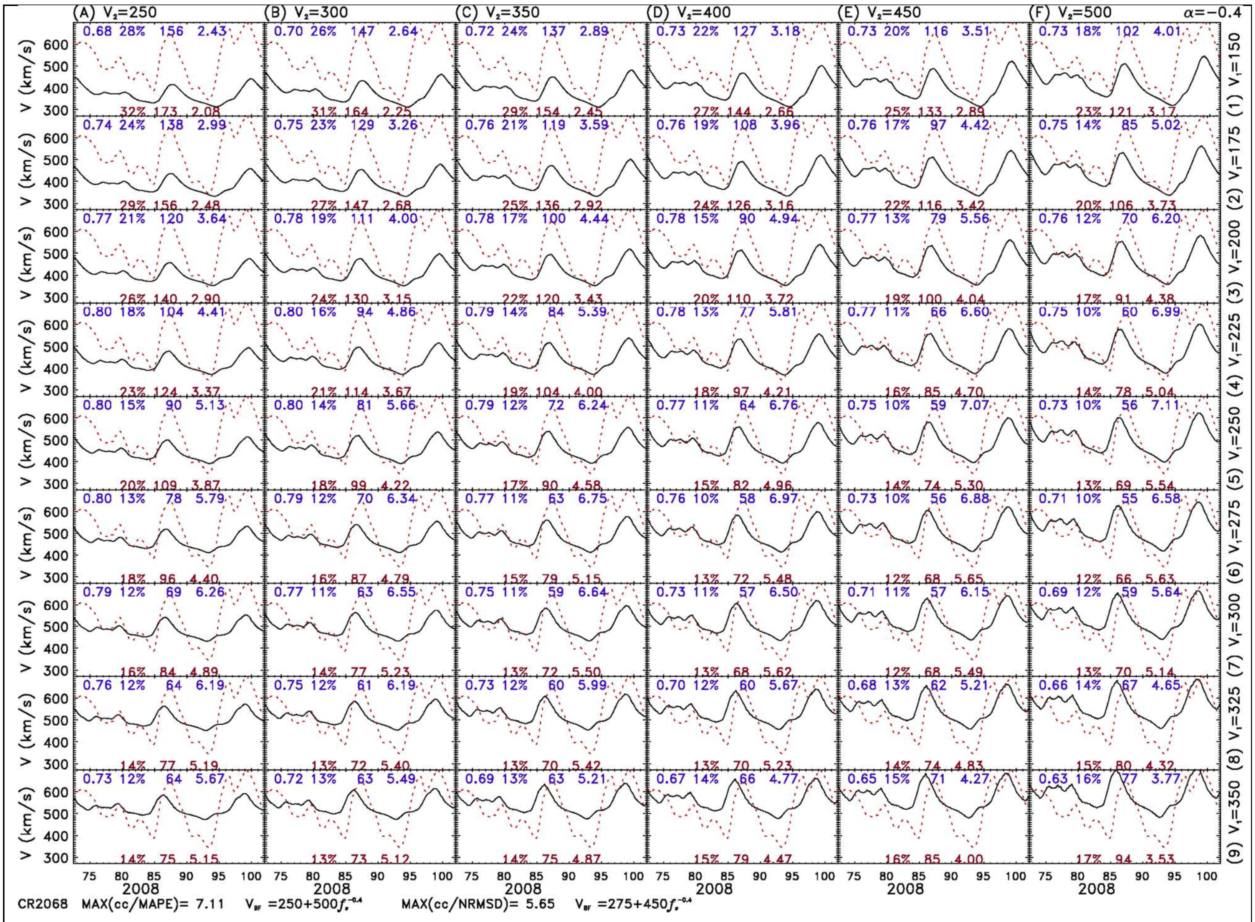

Figure A3. CR2068

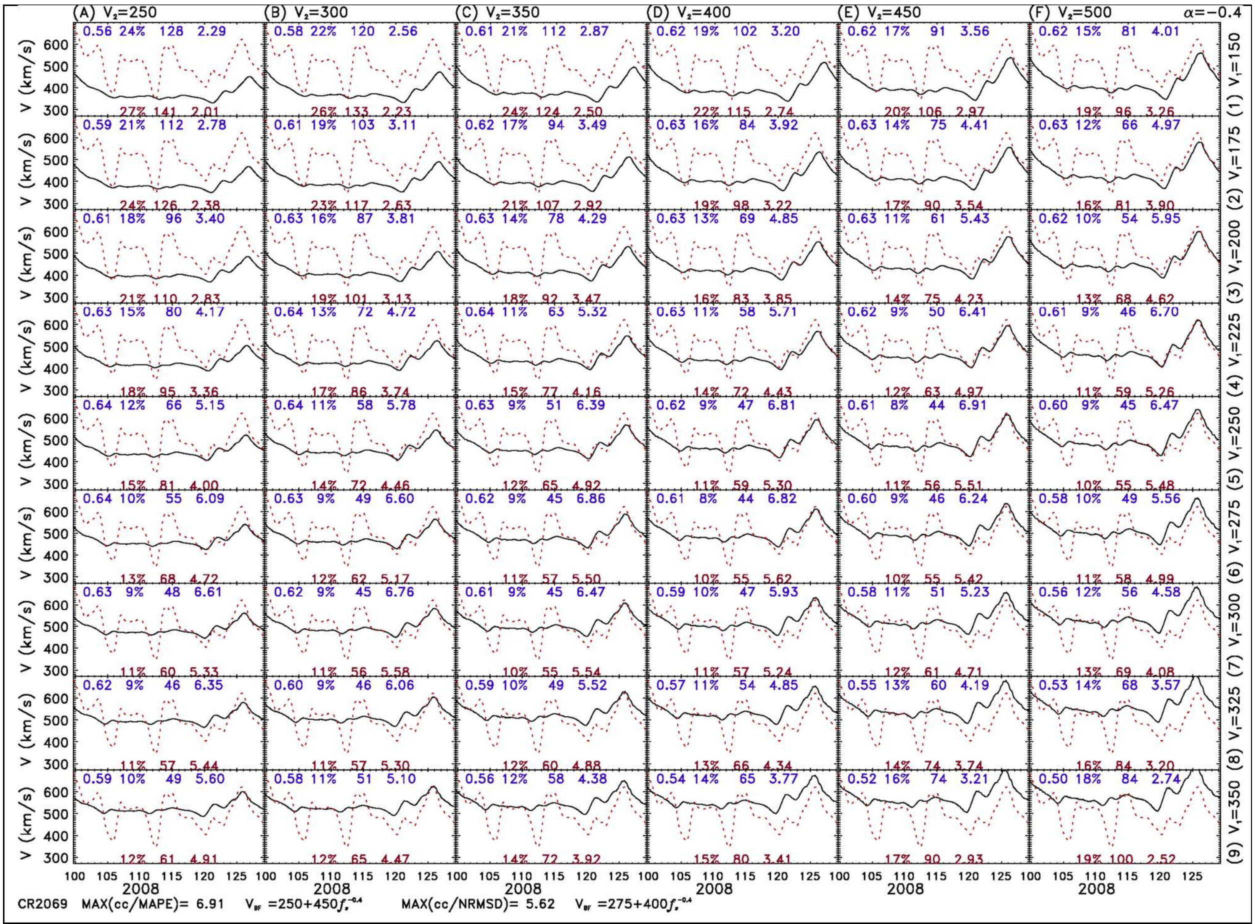

Figure A4. CR2069

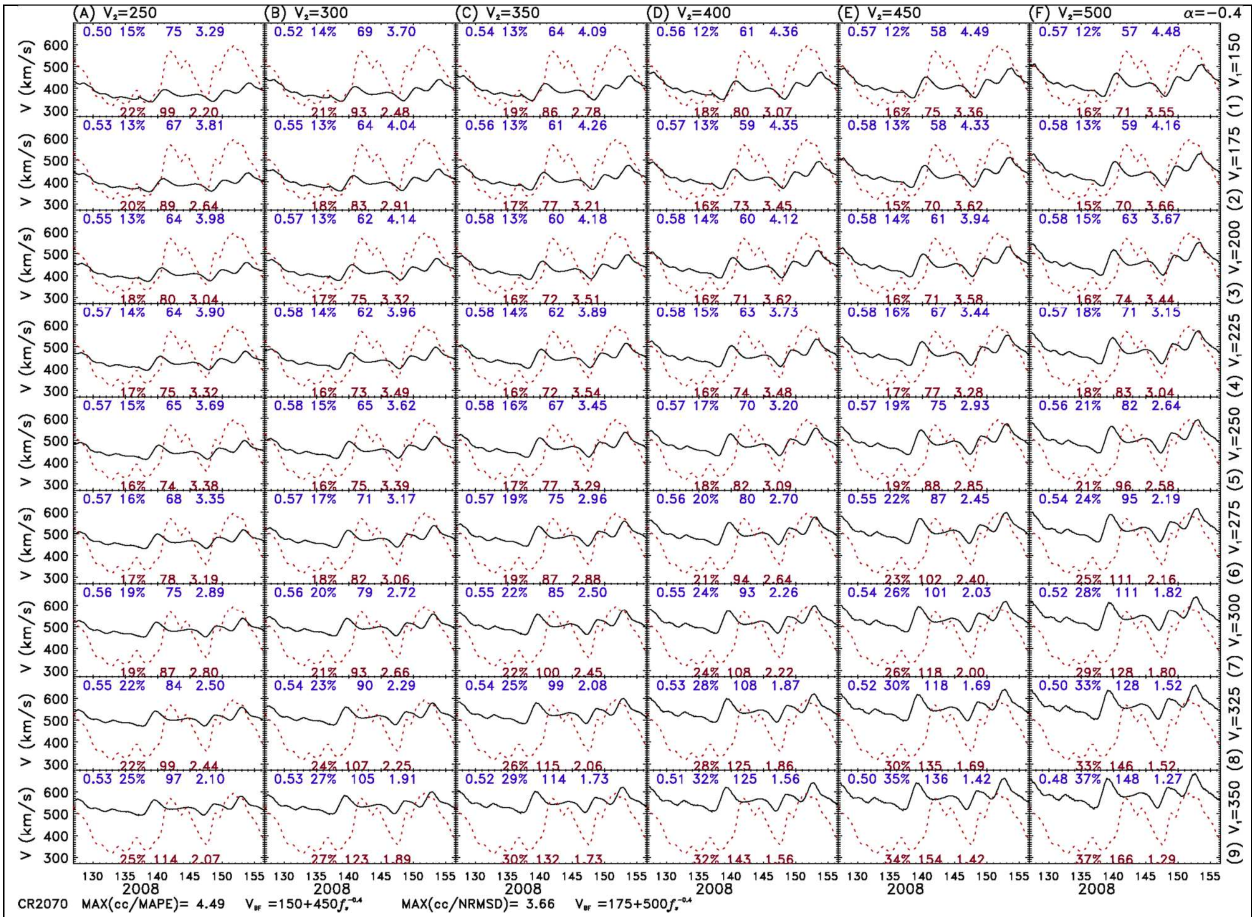

Figure A5. CR2070

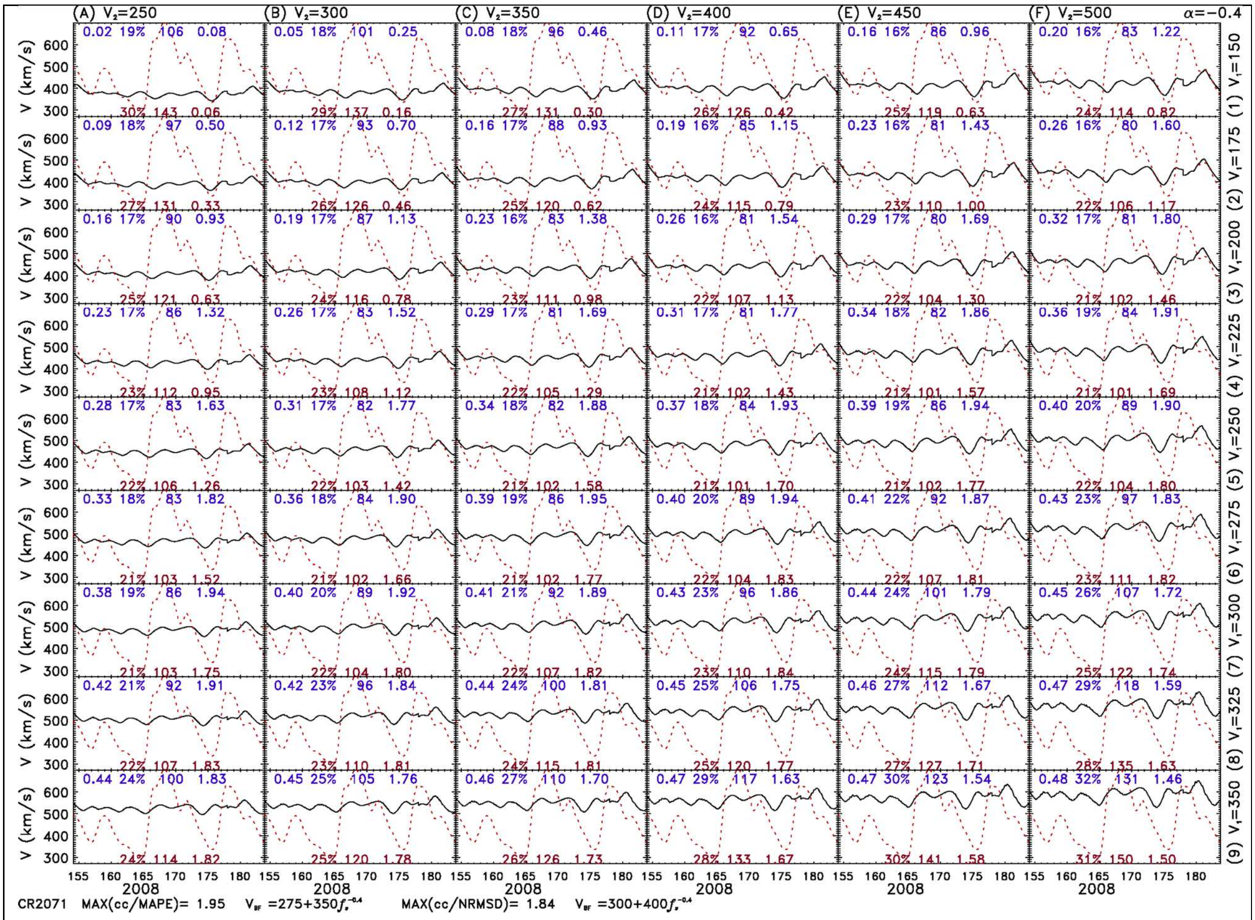

Figure A6. CR2071

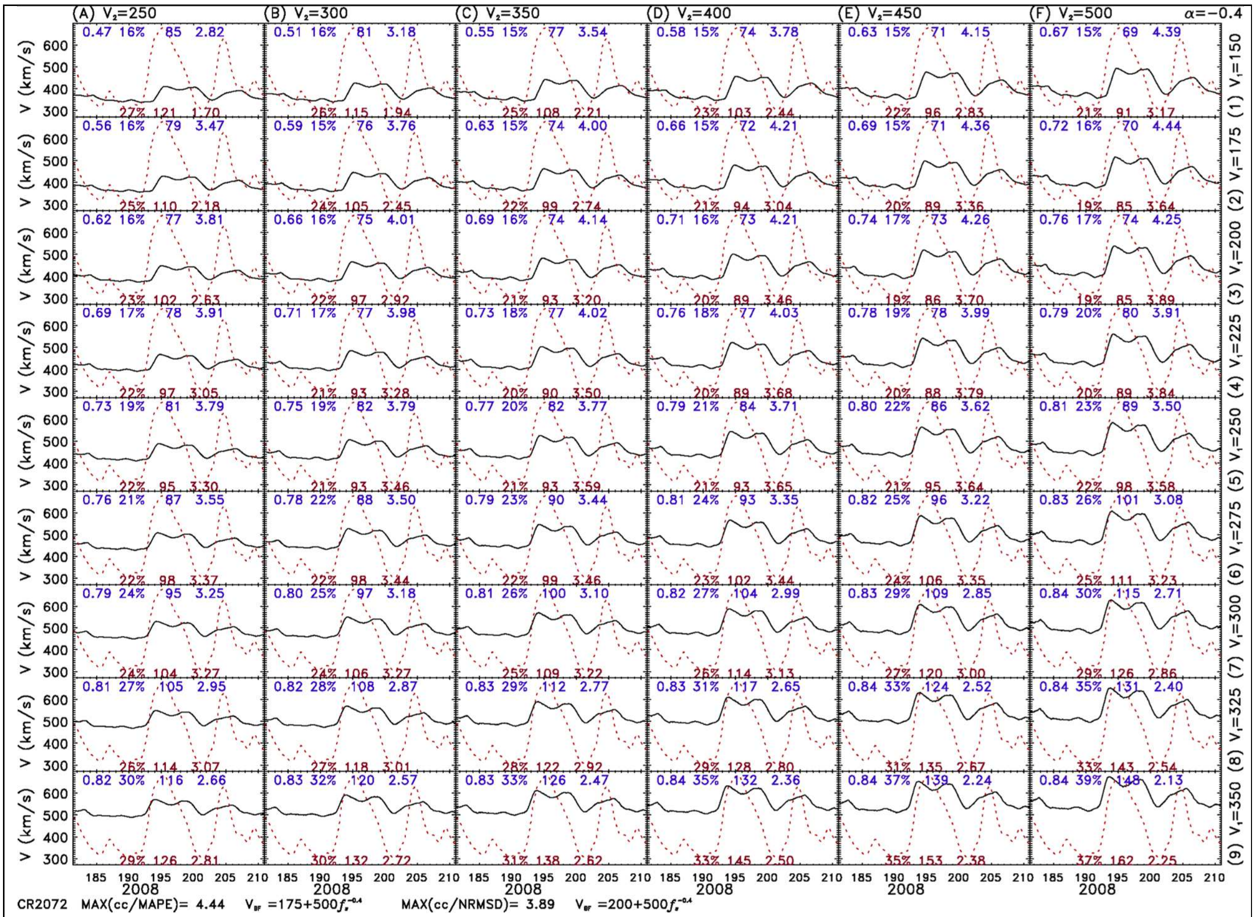

Figure A7. CR2072

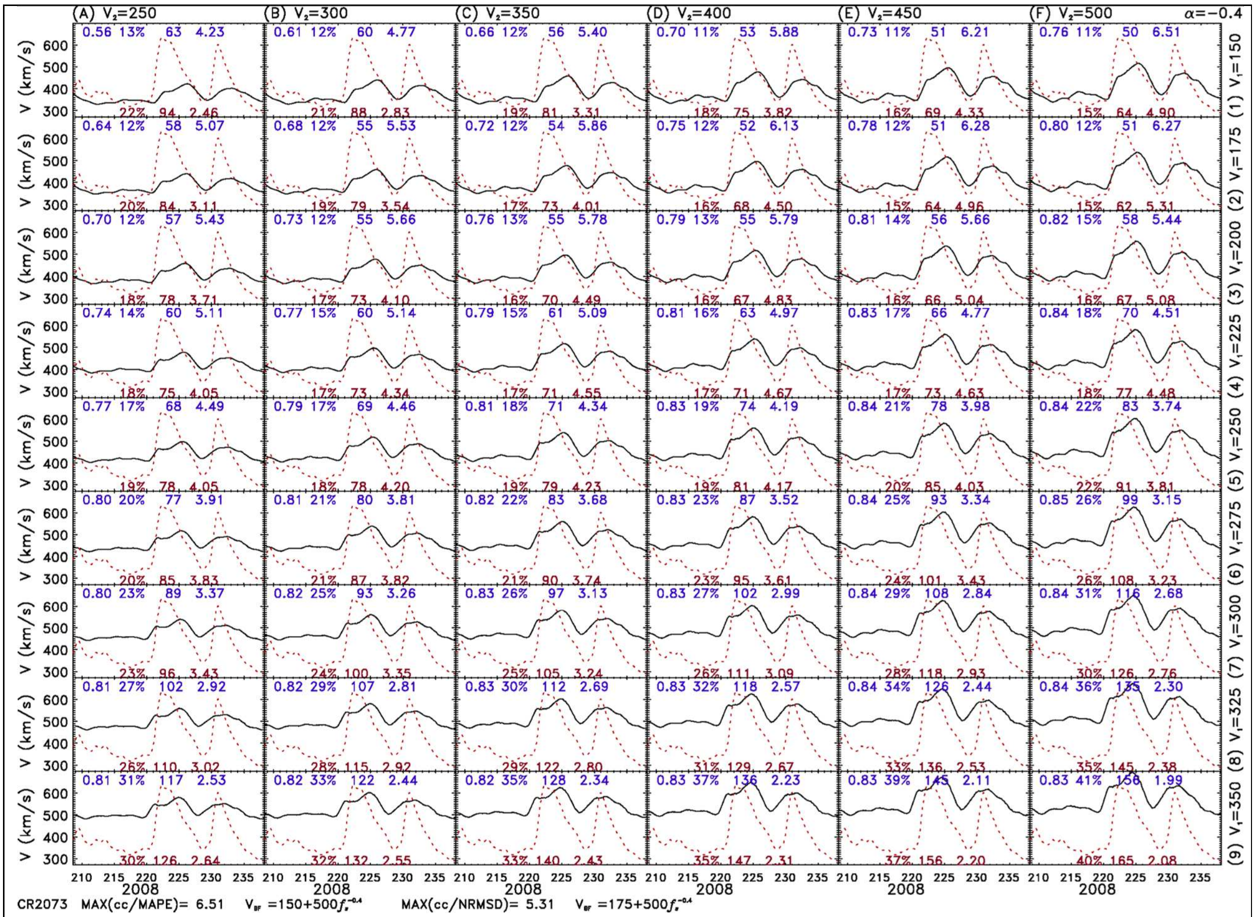

Figure A8. CR2073

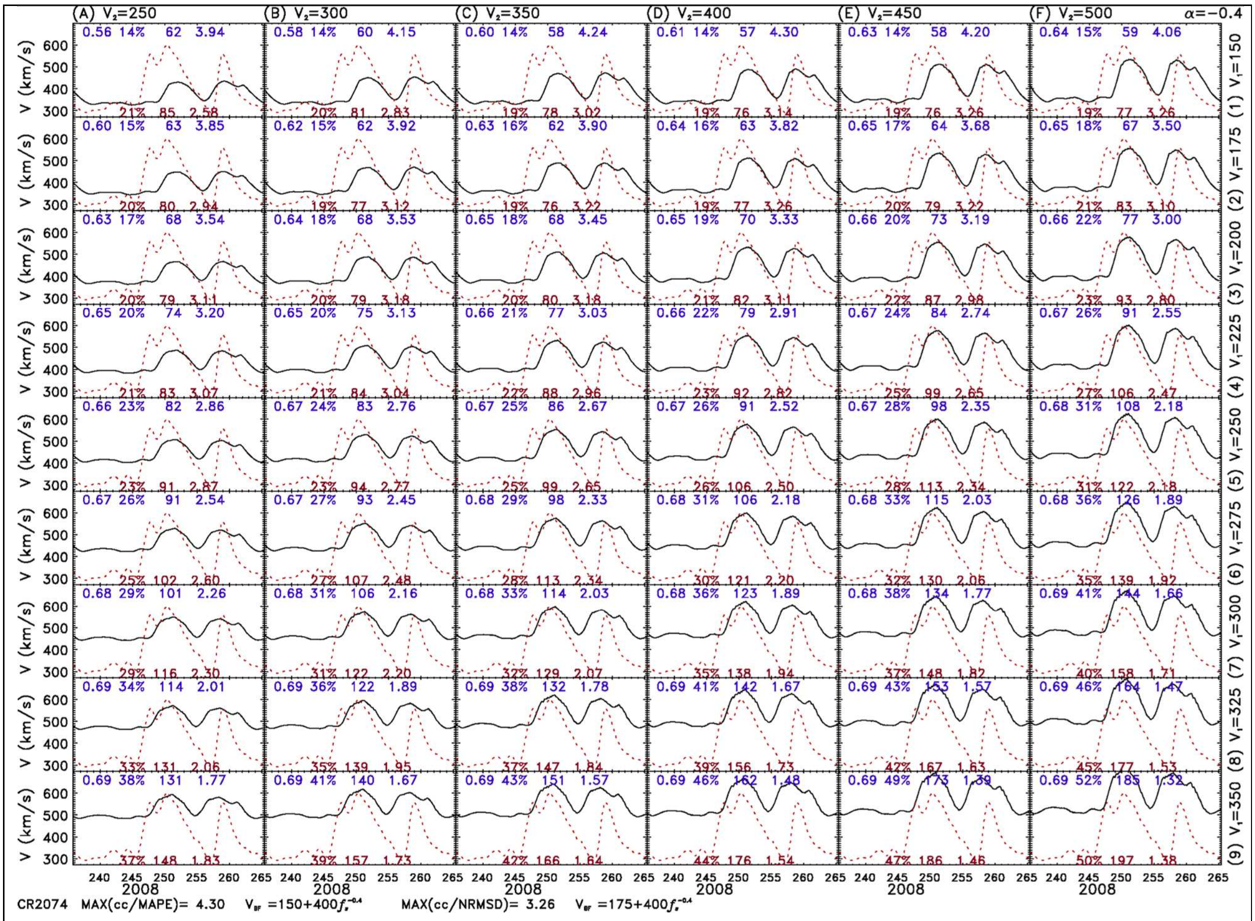

Figure A9. CR2074

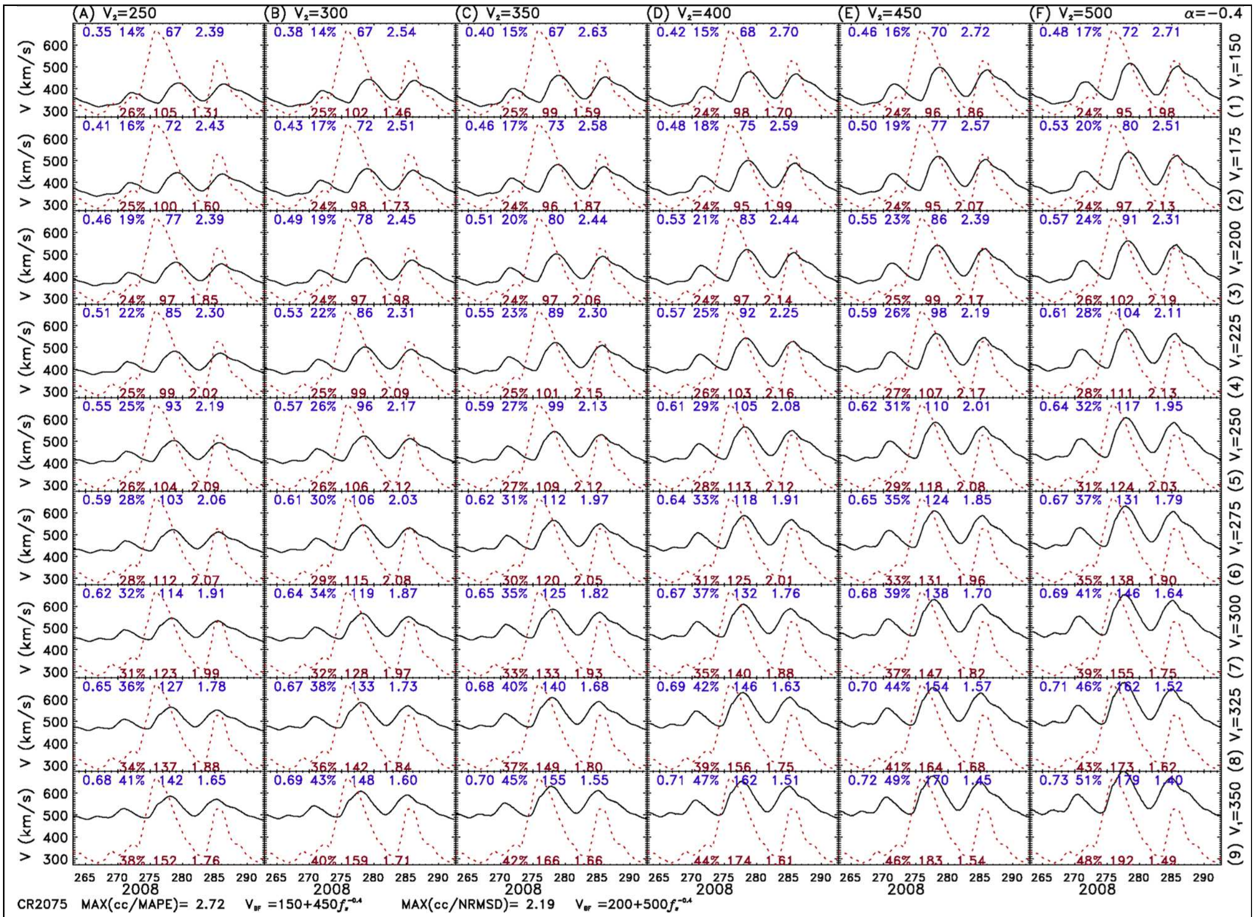

Figure A10. CR2075

743

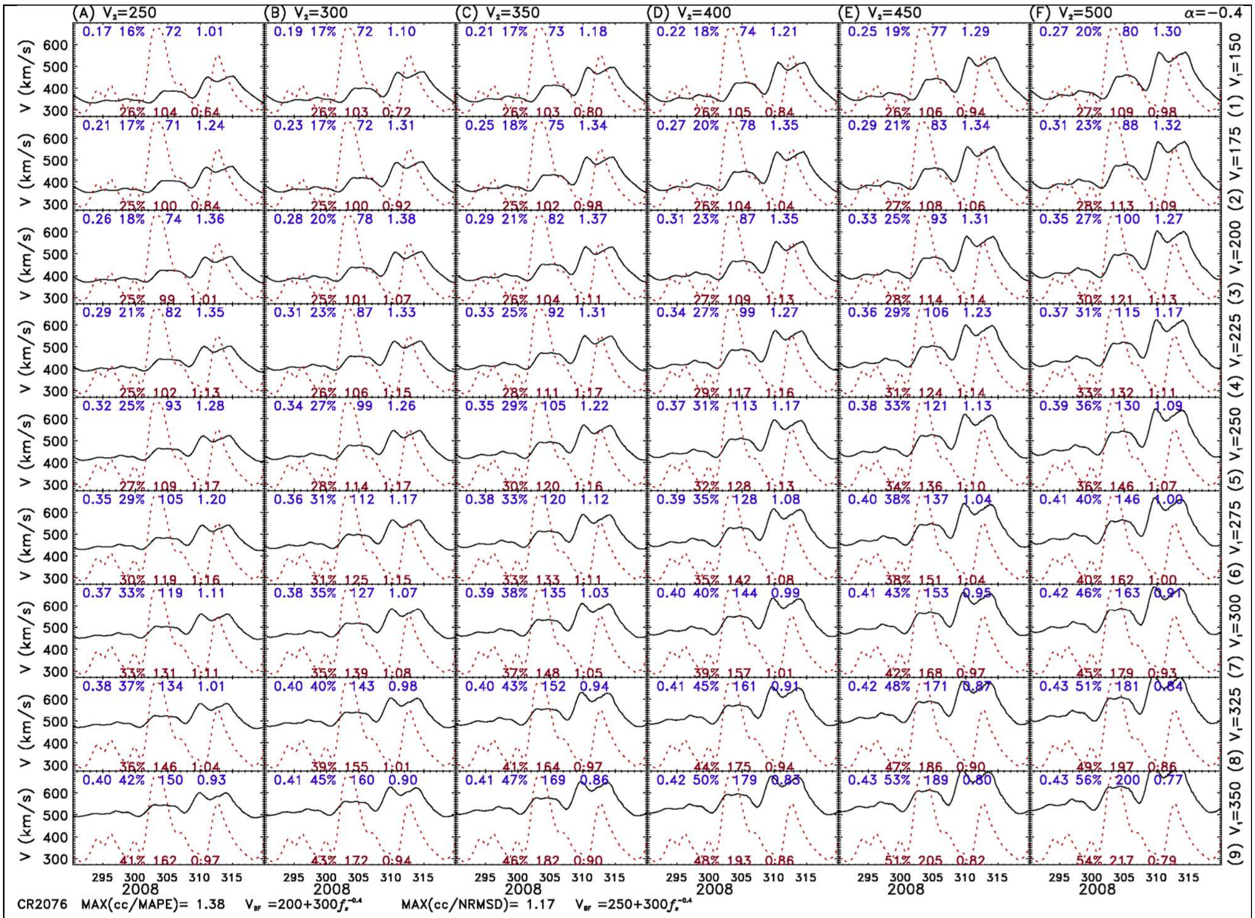

Figure A11. CR2076

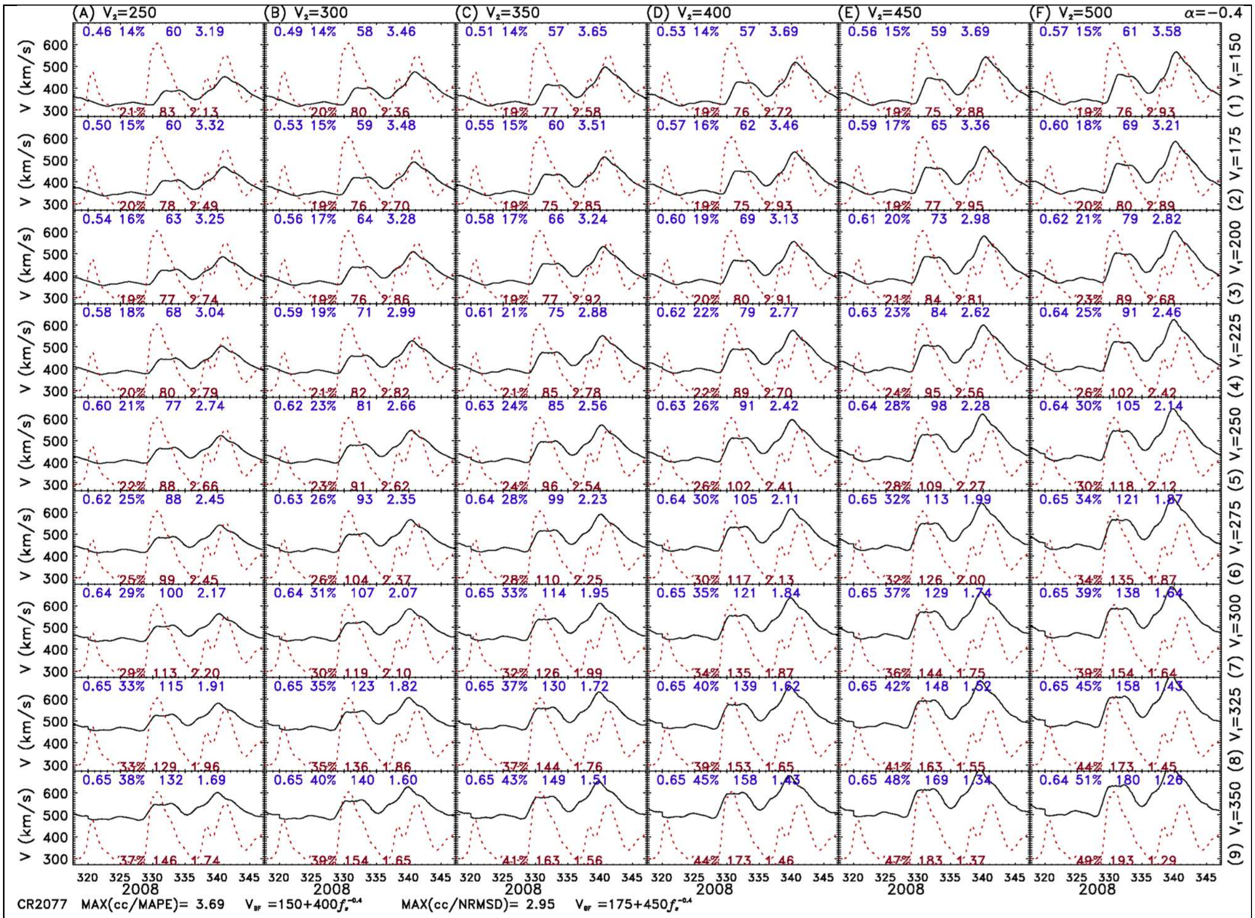

Figure A12. CR2077

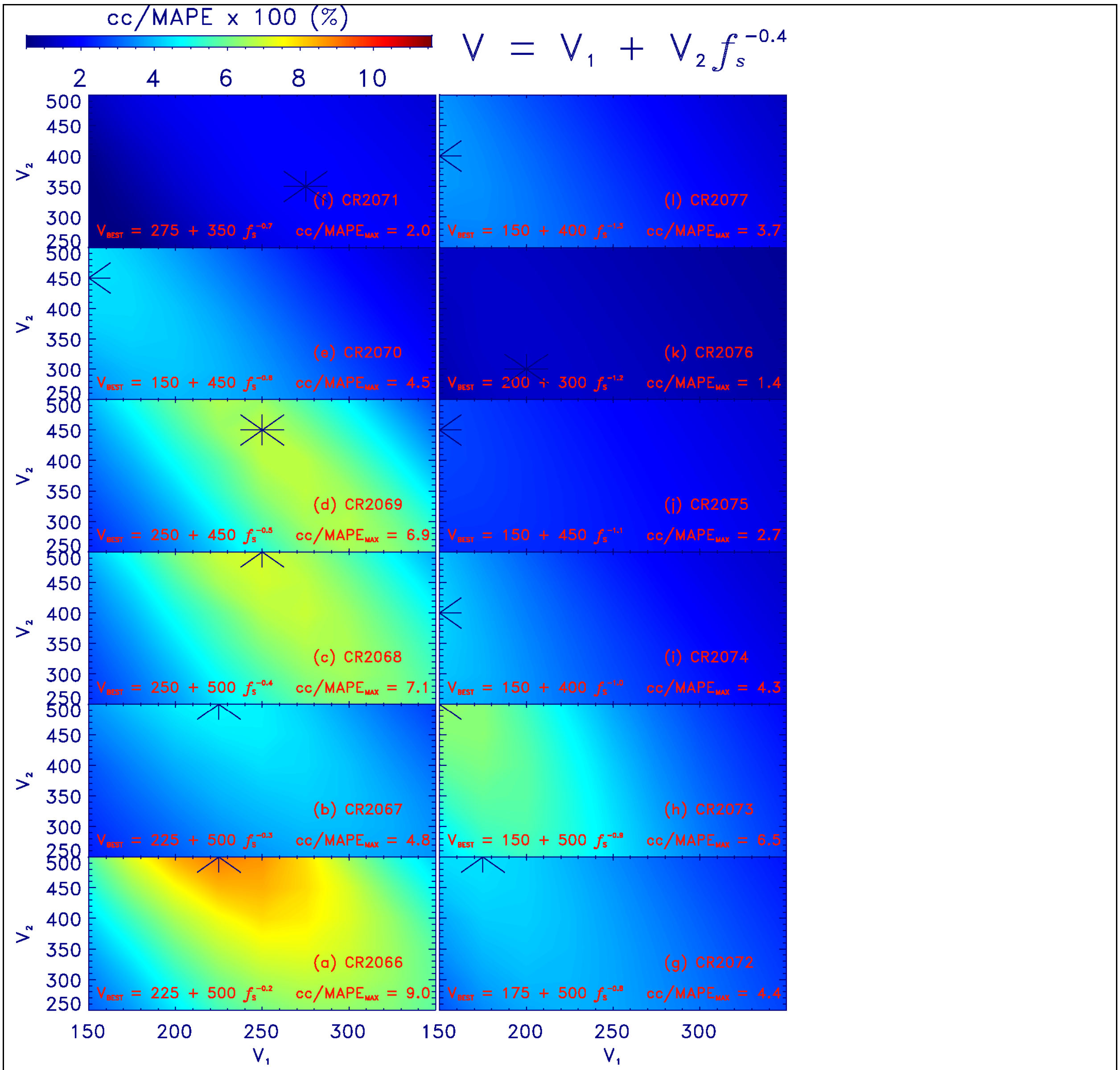

Figure B. Ratio of correlation coefficient [cc] over MAPE for different V_1s (ranges between 150 and 350) and V_2s (ranges between 250 and 500) during 2008 (CR2066-CR2077) using $V = V_1 + V_2 f_s^{-0.4}$. Colors represent the "ratio for the (cc divided by MAPE) × 100 [%]".